

UNIVERSIDAD SAN FRANCISCO DE QUITO USFQ

Colegio de Posgrados

**Transparent Conductive Oxides for Solar Cell Applications: a review and
TCAD simulation approach**

**Tesis en torno a una hipótesis o problema de investigación y su
contrastación**

Kevin Raúl Landázuri Cortez

**PhD. Felice Crupi
Director de Trabajo de Titulación**

Trabajo de titulación de posgrado presentado como requisito
para la obtención del título de Máster en Nanoelectrónica

Quito, 06 de enero de 2023

UNIVERSIDAD SAN FRANCISCO DE QUITO USFQ
COLEGIO DE POSGRADOS

HOJA DE APROBACIÓN DE TRABAJO DE TITULACIÓN

**Transparent Conductive Oxides for Solar Cell Applications: a review and
TCAD simulation approach**

Kevin Raúl Landázuri

Nombre del Director del Programa: Luis Miguel Prócel
Título académico: Doctor of Philosophy
Director del programa de: Maestría en Nanoelectrónica

Nombre del Decano del colegio Académico: Eduardo Alba
Título académico: Doctor of Philosophy
Decano del Colegio: Colegio de Ciencias e Ingenierías

Nombre del Decano del Colegio de Posgrados: Hugo Burgos
Título académico: Doctor of Philosophy

Quito, Enero 2023

© DERECHOS DE AUTOR

Por medio del presente documento certifico que he leído todas las Políticas y Manuales de la Universidad San Francisco de Quito USFQ, incluyendo la Política de Propiedad Intelectual USFQ, y estoy de acuerdo con su contenido, por lo que los derechos de propiedad intelectual del presente trabajo quedan sujetos a lo dispuesto en esas Políticas.

Asimismo, autorizo a la USFQ para que realice la digitalización y publicación de este trabajo en el repositorio virtual, de conformidad a lo dispuesto en la Ley Orgánica de Educación Superior del Ecuador.

Nombre del estudiante: Kevin Raúl Landázuri Cortez

Código de estudiante: 00322947

C.I.: 0401722707

Lugar y fecha: Quito, 06 de enero de 2023.

ACLARACIÓN PARA PUBLICACIÓN

Nota: El presente trabajo, en su totalidad o cualquiera de sus partes, no debe ser considerado como una publicación, incluso a pesar de estar disponible sin restricciones a través de un repositorio institucional. Esta declaración se alinea con las prácticas y recomendaciones presentadas por el Committee on Publication Ethics COPE descritas por Barbour et al. (2017) Discussion document on best practice for issues around theses publishing, disponible en <http://bit.ly/COPETHeses>.

UNPUBLISHED DOCUMENT

Note: The following graduation project is available through Universidad San Francisco de Quito USFQ institutional repository. Nonetheless, this project – in whole or in part – should not be considered a publication. This statement follows the recommendations presented by the Committee on Publication Ethics COPE described by Barbour et al. (2017) Discussion document on best practice for issues around theses publishing available on <http://bit.ly/COPETHeses>.

DEDICATORY

To my family.

Abstract

In the current thesis project, an overview of Transparent Conductive Oxides (TCOs) application for solar cells is presented, with a central focus on four terminal tandem solar cells (4T Tandem). In order to analyze and present the properties of TCOs in solar cells, a literature review and Synopsis Sentaurus TCAD electrical and optical simulations were performed. Since the TCO material most used in solar cells is indium tin oxide (ITO), a comparison between a 4T-tandem using aluminum and ITO as top contacts was analyzed in terms of figures of merit and performance. Finally, it is presented a discussion of the trade-off between transparency and electrical conductivity of ITO contacts by varying the width and thickness and analyzing the trends of optimization.

Key words: Transparent, conductive-oxides, solar-cells, TCOs, synopsis, Sentaurus, electrical, optical, simulations, contacts, transparency, conductivity, optimizations.

CONTENTS

<i>Dedicatory</i>	5
<i>Abstract</i>	6
<i>Introduction</i>	13
<i>Chapter 1: fundamentals of physics for solar applications</i>	16
1.1 Solar Radiation.....	16
1.1.1 The Sun.....	16
1.1.2 Blackbody radiation.	17
1.1.3 Solar spectra and Air Mass	18
1.2 Fundamentals of semiconductors	20
1.2.1 Basic physics.....	20
1.2.2 Carriers	25
1.2.3 Doping	27
1.2.4 Fermi Level.....	29
1.2.5 Carrier transport.....	30
1.3 Photoelectric effect.....	31
1.3.1 The wave-particle duality	31
1.3.2 Photovoltaic effect.....	32
<i>Chapter 2: solar cells</i>	33
2.1 Solar cell working principle.....	33
2.2 Generation and recombination	34
2.2.1 Direct bandgap processes.....	35
2.2.2 Radiative recombination.....	36
2.2.3 Auger recombination	37
2.2.4 Shockley-Read-Hall recombination	38
2.2.5 Surface Recombination	39
2.3 Parameters of a solar cell	40
2.3.1 I-V characteristic.....	40
2.3.2 Short-circuit current ISC.....	42
2.3.3 Open circuit voltage VOC.....	43
2.3.4 Fill Factor	43
2.3.5 Energy-conversion efficiency	44
2.4 Progress and performance of solar cells.....	45
2.4.1 Single-crystalline cells.....	45
<i>Chapter 3: Transparent conductive oxides</i>	53
3.1 Indium-Tin Oxide (ITO).....	54
3.2 Transparent electrodes: conventional TCO films	58
3.3 TCOs used in tandem cells	60
<i>Chapter 4: Simulations of 4T Tandem solar cell with ITO</i>	64
4.1 Sentaurus TCAD.....	64
4.2 Introduction of ITO in Sentaurus	67
4.3 4T Tandem cell simulation	70
4.4 GaAs cell simulation.....	71

4.4.1	Electric/Optic GaAs cell simulation	72
4.5	Silicon bottom cell simulation	74
4.5.1	IV bottom cell simulation	78
4.6	Results on tuning parameters	79
4.7	Overall figures of merit for a 4T tandem solar cell with ITO contacts.....	84
<i>Conclusions</i>		<i>85</i>
<i>References</i>		<i>87</i>

LIST OF TABLES

Table 1. 1: Carrier concentration in most common intrinsic semiconductors at 300 K, adapted from (Michalopoulos, 2002)	27
Table 4. 1: Figures of merit for Al and ITO top cell configuration	73
Table 4. 2: Figures of merit Al and ITO top cell	79
Table 4. 3: Values used to sweep the variables on the ITO contacts	80
Table 4. 4: Values used to sweep the thickness of the ITO contacts	82
Table 4. 5: Final figure of merit of a 4T tandem solar cell using ITO as contacts	84

LIST OF FIGURES

Figure 1. 1: Structure of the Sun (adapted from (NASA, 2012)).....	16
Figure 1. 2: Sun's spectrum compared like an imperfect blackbody as predicted by Smerlak (2011).....	18
Figure 1. 3: Solar spectra for blackbody at 6000 K, the extraterrestrial AM0 spectrum and AM1.5 spectrum. Adapted from: Smets et al.(2015).	19
Figure 1. 4: Air Mass coefficient calculation in different scenario.....	20
Figure 1. 5: Resistivity comparison for a variety of materials (Simon, Yiming, & Kwok, 2021).....	21
Figure 1. 6: Electron transition from lower to higher shells (left) and from higher to lower shells (right).....	21
Figure 1. 7: Conductivity vs. Temperature	22
Figure 1. 8: Energy levels and orbitals.....	23
Figure 1. 9: Energy bands for typical materials. (a) Insulator. (b) Conductor. (c) Semiconductor. Adapted from (Kalogirou, 2013).....	24
Figure 1. 10: Periodic table of elements, adapted from (Base, 2021)	25
Figure 1. 11: Electron disposition in a semiconductor.....	26
Figure 1. 12: Intrinsic carrier density vs. Temperature adapted from (Michalopoulos, 2002).27	27
Figure 1. 13: Structures of N-type and P-type semiconductor dopings. Adapted from (Michalopoulos, 2002).....	28
Figure 1. 14: Fermi-Dirac distribution for different temperatures (Basnet, 2015).	30
Figure 1. 15: Diffusion current produced by the movement of the carriers (Michalopoulos, 2002).....	30
Figure 1. 16: Drift current produced by an external electromagnetic field (Michalopoulos, 2002).....	31
Figure 1. 17: Photoelectric effect: electrons are emitted from matter (Learning, 2022).....	32
Figure 2. 1: Absorption of photons in semiconductors (a), and its posterior effect of thermalization (b). Adapted from (Smets et al. ,2015).....	33
Figure 2. 2: Simple solar cell model. (Smets et al.,2015)	34
Figure 2. 3: Electronic dispersion diagram for (a) direct bandgap and (b)indirect bandgap semiconductors. (Smets et al.,2015).....	35
Figure 2. 4: Radiative generation (a) and recombination (b) for direct bandgap semiconductors.	36
Figure 2. 5: Auger recombination with the presence of (a) two electrons; and (b) two holes. 37	37
Figure 2. 6: SRH recombination for (a) donor-type; and (b) acceptor-type traps.....	39
Figure 2. 7: I-V characteristic of a solar cell under dark and illuminated conditions.....	41
Figure 2. 8: Theoretical limit on photogenerated current in comparison with the best measured values, at AM1.5 photon flux (McEvoy & Markvart, 2003).....	42
Figure 2. 9: Fill factor represented in the IV characteristic curve (Bartesaghi, et al., 2015) ...	44
Figure 2. 10: Efficiency Shockley-Queisser limit. Adapted from (Smets, et al., 2015)	45

Figure 2. 11: Device architectures of different types of c-Si single cells. Adapted from (Nayak, Mahesh, Snaith, & Cahen, 2019).....	46
Figure 2. 12: Device architectures of different types of GaAs cells. Adapted from (Nayak, Mahesh, Snaith, & Cahen, 2019).....	47
Figure 2. 13: Efficiency comparison between a single-junction and double- junction solar cells. Adapted from (Bailie, 2015)	48
Figure 2. 14: Scalable tandem architectures. Adapted from (Bailie, 2015)	49
Figure 2. 15: Different multijunction configurations, organized by the number of electrical terminals. Adapted from (Martinho, 2021)	50
Figure 3. 1: Mass fraction abundance of the elements in the Earth’s crust as a function of atomic number. Common TCO cations are highlighted by colored circles and additional dopants by squares. Adapted from (Kalowekamo & Baker, 2009).....	53
Figure 3. 2: Electrical resistivity and carrier concentration of ITO at different tin concentration (wt%). Adapted from (Mryasov & Freeman, 2001)	55
Figure 3. 3: Simplified band structures of pure indium oxide In ₂ O ₃ (left) and ITO (right). Adapted from (Gupta, A., & Srivastava, 1989).....	57
Figure 3. 4: Optical constants n(solid line) and k(dotted line) of ITO. Obtained from (Gupta, A., & Srivastava, 1989)	57
Figure 3. 5: Overview of photovoltaic devices using transparent conductive layers. Reproduced from (Delahoy & Guo, 2011)	59
Figure 3. 6: Reported properties of n-type transparent conducting oxides. Re- produced from (Dekkers, 2007).	60
Figure 3. 7: Schematic structure of the perovskite solar cells using ITO. Reproduced from (Bett, et al., 2019)	61
Figure 3. 8: Schematic diagram of the a-Si:H/uc-Si:H tandem tin film solar cells using ITO. Reproduced from (Leem & Su, 2011)	61
Figure 3. 9: Different configuration on solar cells architectures and D) absorption spectra of thick evaporated MoOx. Reproduced from (Leem & Su, 2011)	62
Figure 4. 1: Sentaurus TCAD workbench graphical environment.....	65
Figure 4. 2: Sentaurus Device Editor with a simple 2D MOSFET.....	66
Figure 4. 3: Sentaurus Device in a complete analysis of a solar cell.	67
Figure 4. 4: Implementation of ITO in Sentaurus device editor.	68
Figure 4. 5: Current-voltage characteristics of p-type c-Si wafer/ITO junctions (Das & Karmakar, 2019).....	68
Figure 4. 6: ITO/c-Si single junction performed in Sentaurus.	69
Figure 4. 7: Sdevice section to introduce ITO material.	69
Figure 4. 8: Current-voltage curve obtained for the structure given in Figure 4.7	70
Figure 4. 9: Schematic of the simulated 4T tandem solar cell in TCAD Sentaurus.	70
Figure 4. 10: Variation on front contact ITO width (5-20-150 μm) in top cell.....	71
Figure 4. 11: Variation on bottom contact ITO width (5-50-150 μm) in top cell.....	72
Figure 4. 12 I-V curves for a top GaAs solar cell using Aluminium and ITO as top contact :	72

Figure 4. 13: Transmittance spectra of aluminum and ITO-based solar cells.....	74
Figure 4. 14: AM1.5g spectrum and GaAs cell output spectrum using ITO as top contact. ...	74
Figure 4. 15: 2D symmetry element of c-si solar cell	75
Figure 4. 16: Silicon parameters for the optic simulation of bottom cell.....	77
Figure 4. 17: Structure of the silicon bottom cell.....	78
Figure 4. 18: I-V characteristic for the bottom cell configuration using ITO and Al as contacts	79
Figure 4. 19: Figures of merit variations due the sweep of the front contact width.	81
Figure 4. 20: Figures of merit variations due the sweep of the bottom contact width.....	82
Figure 4. 21: Figures of merit variations due to the variation of the top contact width of bottom cell width.	83

INTRODUCTION

The consumption of electrical power due to human activities has grown exponentially in the last few years. The world power demand in the 1980s was around 7 *KTW*, but increased up to 18 *KTW* in the 2010s, and reached approximately 23 *KTW* in 2019. The electrical demand is supplied by a variety of sources such as coal, nuclear energy, and hydroelectricity, among others. However, the conversion of energy from fossil fuels power plants comes with the disadvantages of the contribution to global warming and the limit of such natural sources. To overcome those limitations, several efforts in the field of renewable energy sources have been made. One of the most promising sources of energy is related to the conversion of solar energy into electrical energy, due to the relatively unlimited amount of available free-contamination energy.

The most widely studied method to convert solar energy into electric energy is the photovoltaic technology. Over time, the research in photovoltaic (PV) systems has focused on two directions. The first one is related directly to the economical aspect, in which technologies must be limited to the use of cheap materials, or at least, materials that can replace the common sources of energy at a comparable cost. In this regard, crystalline solar cells are the most exploited and thereby, the most fabricated ones. On the other hand, the second approach is driven by the goal of obtaining the maximum possible efficiency, which is basically the capability of a PV system to convert the solar energy into usable electric energy. Nevertheless, there are theoretical limitations (such as the Shockley-Queisser limit) that systems with single junctions cannot overcome.

In the last decades, PV systems optimizations were studied in order to provide different technologies, materials, and architectures that ended up overcoming the limits of single junction cells. In this ambit, technologies such as multijunction cells (widely known as tandem cells)

were developed, with the idea that it is possible to join two different but electrically connected cells, with the advantage of increasing the efficiency of the overall system. This thesis is based on the architecture called four-terminal (4T) tandem solar cell, in which was studied and implemented a specific category of materials called *transparent conductive oxides* (TCOs). These are transparent materials able to conduct electricity, and so this characteristic was used to reduce the effect of shadowing produced by metallic contacts, which is one of the main sources of losses in solar cells.

In this project, two approaches were followed. The first comprehends an overview of the TCOs in solar cells, reporting a variety of materials and configurations, its working principle, and the state of the art with a special focus on the 4T tandem cells. The second objective was the development of Sentaurus-TCAD simulations of a 4T tandem cell, in which one of the most used TCO materials, known as *indium-tin oxide* (ITO), was implemented and studied.

The **first chapter** presents the theoretical aspects of physics for application in the field of solar cells. An overview of solar radiation, its spectra, properties, and basic on semiconductors are also addressed. The **second chapter** provides an explanation of solar cells in general, their working principle, the recombination processes that occur in PV systems, and figures of merit. The concluding section of this chapter focuses on the progress in the solar cell architectures, analyzing the single-junction crystalline systems and the central topic of this research, the tandem cells.

The **third chapter** contains the state of the art of transparent conductive oxides and their advantages in the field of solar cells. Furthermore, it is provided an overview on the various TCOs used in PV architectures, their optical and electrical behavior, and an investigation on their implementation in tandem solar cells.

The **fourth chapter** comprises the implementation of ITO in Sentaurus-TCAD simulations, specifically in a 4T tandem cell using as top cell a GaAs thin-film solar cell and as bottom one

a single-junction crystalline cell. The first section describes the TCAD software used in this work and the methodology in which the simulations were performed. In the second section are presented the results in terms of variations of the geometrical aspects of ITO as a contact in a 4T tandem cell with their impact on the figures of merit. Finally, the conclusions will highlight the results of the review and experimental sections and present possible future works on the subject.

CHAPTER 1: FUNDAMENTALS OF PHYSICS FOR SOLAR APPLICATIONS

1.1 Solar Radiation

1.1.1 The Sun.

Solar energy is generated in the central star of our system, the sun, and it is constituted mainly of hydrogen and helium. In the center of the sun, the extraordinary conditions of both temperature ($\sim 15 \times 10^6 \text{ K}$) and pressure ($\sim 1 \times 10^{12} \text{ atm}$), produce thermonuclear reactions that release an enormous amount of energy. Specifically, a nuclear proton-proton reaction, produces one helium core, two positrons, two neutrinos and electromagnetic radiation. The last one, produced at the core (see **Figure 1.1**), is not visible since it is absorbed by a layer of hydrogen.

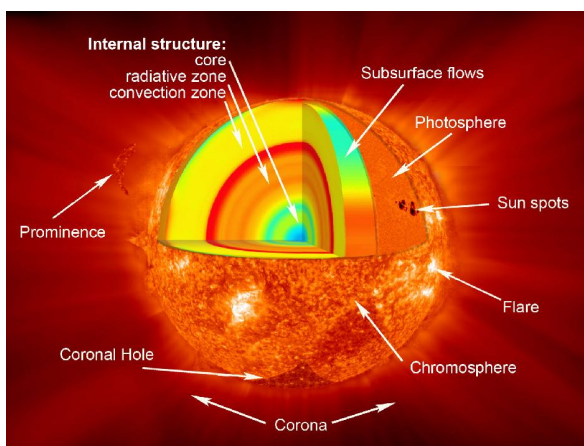


Figure 1. 1: Structure of the Sun (adapted from (NASA, 2012))

The total power of energy radiation emitted by the sun is approximately $3.8 \times 10^{26} \text{ W}$, of which the portion received by the Earth is about $1.7 \times 10^{28} \text{ W}$. At the surface of the Earth, approximately a 30% of the incoming power is reflected back to space, in addition to the absorption by clouds, oceans and land masses (Smets, Jägger, Isabella, Swaaij, & Zeman, 2015). Even with the inclusion of all the losses, the Earth receives in one hour more energy than the one consumed in one year by the entire human population. This evaluation alone qualifies the solar energy as one of the primary sources of energy to exploit, even more so considering its renewable nature (Callozzo, 2011).

1.1.2 Blackbody radiation.

The concept of a blackbody object is very useful to understand the thermal radiation mechanism. This behavior is theoretical in principle, since one of its properties is that it absorbs all the incident radiation onto it and thereby it will emit electromagnetic radiation. Several efforts have attempted to calculate the blackbody spectrum, but the one that was found to be the most accurate is given in **Eq.1.1**, and it is called the *Planck's Law*.

$$B_{\lambda}(T) = \frac{2hc^2}{\lambda^5} \frac{1}{e^{\frac{hc}{\lambda K_B T}} - 1} \quad (1.1)$$

From such law it is possible to observe the dependency of the spectral radiance from the temperature of the blackbody, where the other constants are $c = 2.99 \times 10^8$ [m/s], the speed of light in vacuum, $K_B = 1.38 \times 10^{-23}$ [J · K⁻¹], the Boltzmann constant, and $h = 6.63 \times 10^{-34}$ [J · s], the Planck's constant.

Considering the case of long wavelengths, it is possible to apply the following approximation:

$$\exp\left(\frac{hc}{\lambda K_B T}\right) - 1 \approx \frac{hc}{\lambda K_B T} \quad (1.2)$$

Integrating the spectral radiance over all wavelengths the total radiant emittance of blackbody is found, shown in **Eq.1.3**. It's notable the relation of the emittance with the temperature, that implies that an increase in temperature will have a relevant impact over the total emitted power.

$$I = \sigma T^4 \quad (1.3)$$

Where σ is the *Stefan-Boltzmann* constant, given as:

$$\sigma = \frac{2 \pi^5 (K_B)^4}{15 c^2 h^3} \approx 5.67 \times 10^{-8} \frac{W}{m^2 K^4} \quad (1.4)$$

Those definitions for a blackbody are introduced since the surfaces of both the Sun and the Earth are considered approximately to behave as blackbodies. Thereby, the solar spectral irradiance can be approximated using previous relation, providing a certain temperature, known as effective temperature. Considering a range of temperatures between 5500 and 6000 K, the solar spectrum can be well approximated as it is shown in **Figure 1.2** (Smerlak, 2011). The total radiation that the Earth receives in the space is almost constant, but it will vary on the surface due to the effects previously introduced, for example the atmospheric absorption.

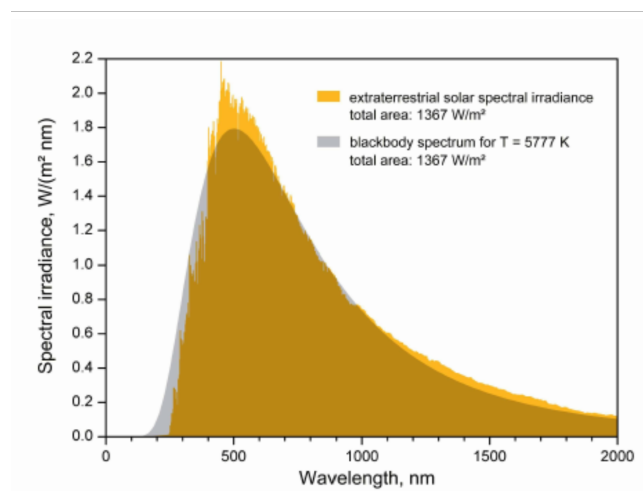


Figure 1. 2: Sun's spectrum compared like an imperfect blackbody as predicted by Smerlak (2011)

1.1.3 Solar spectra and Air Mass

The spectrum emitted by the Sun, as stated in the previous section, could be well approximated using the *Planck's law*, treating it as a perfect blackbody. In order to determine the spectral irradiance that Sun would have on Earth, is necessary to include the solid angle between them, given as:

$$\Omega_{SUN} = \pi \left(\frac{R_{SUN}}{Au - R_{EARTH}} \right)^2 \approx 68.5 \text{ usr} \quad (1.5)$$

Where $R_{SUN} = 696,000 \text{ km}$ is the radius of the Sun, $Au = 140,600,00 \text{ km}$ is the astronomical unit, and the radius of the Earth is given as $R_{EARTH} = 6,370 \text{ km}$. With such

information is possible to observe the differences between the perfect blackbody spectrum and the sun's one.

Solar Spectra

Figure 1.3 shows the comparison of the blackbody spectrum calculated at 6000K, with the AM0 and AM1.5 spectra. The former is defined as the spectrum received from the Earth in space, without considering the atmospheric effects. The latter requires a comprehension of how the radiation is going through the atmosphere of the Earth, and therefore is attenuated. The factor that determines or characterizes the path of radiation going through the atmosphere is known as Air Mass (AM).

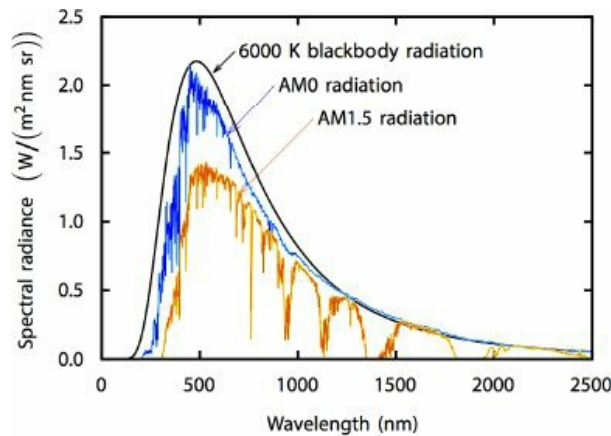


Figure 1. 3: Solar spectra for blackbody at 6000 K, the extraterrestrial AM0 spectrum and AM1.5 spectrum. Adapted from: Smets et al.(2015).

Air Mass (AM)

Air Mass coefficient provides information about the path that light follows while traversing the atmosphere. It is defined as the ratio between the total path of light over the minimum path possible, obtained when the sun it is at zenith position (sky directly overhead). The definition of AM is given in **Eq.1.6**, where θ is the zenith angle.

$$AM = \frac{TotalLightPath}{MinimumLightPath} = \frac{1}{\cos \theta} \quad (1.6)$$

This relation provides a measurement of how much the power is reduced when light passes through different scenarios. Increasing the AM coefficient means lower the intensity of

sunlight. Another way to obtain the AM coefficient is considering the shadowing that an obstacle produces, as it is depicted in **Figure 1.4**.

$$AM = \sqrt{1 + \left(\frac{s}{h}\right)^2} \quad (1.7)$$

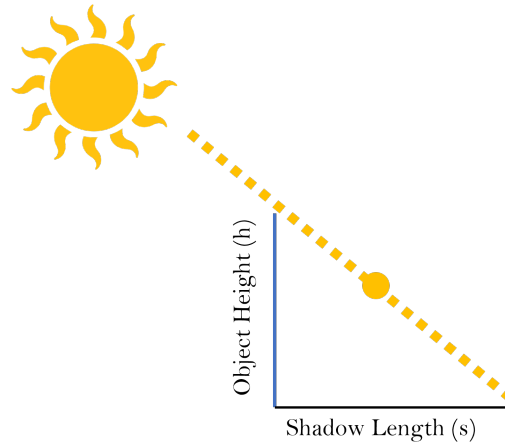


Figure 1. 4: Air Mass coefficient calculation in different scenario.

In specific cases, as in the design of solar cells, this factor becomes vital since the design of such cells depend on the availability of solar insolation at certain locations. So, since the conditions around the Earth will vary, there exists standard conditions. The standard air mass conditions are the AM1.5, known as ASTM G173-03, having the data regarding annual average solar irradiation, as being $1000 [W \cdot m^2]$, and angles θ of 48.19 (Callozzo, 2011), (International, 2021). These values concern locations as Europe, China, United States, among others. In contrast, the Sahara's irradiation average value goes to $2,200 [W \cdot m^2]$, which will be ideal in terms of insolation but with much harsher ambient conditions.

1.2 Fundamentals of semiconductors

1.2.1 Basic physics

It is possible to categorize the materials found in nature according to their electrical properties. Broadly speaking, three types of electrical behaviors exist, *conductors*,

semiconductors, and *insulators*. Among the most important electrical properties that make materials to behave electrically different there are *resistivity* ρ and *conductivity* σ ; **Figure 1.5**, shows both resistivity and conductivity for some type of materials.

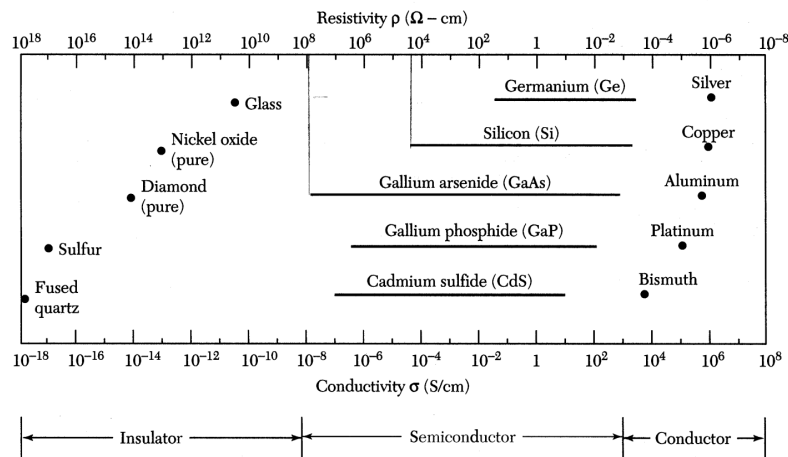


Figure 1. 5: Resistivity comparison for a variety of materials (Simon, Yiming, & Kwok, 2021).

Essentially, all materials are composed by atoms tight one to each other by bonds (ionic, covalent, and metallic). Within each atom, a nucleus containing protons and neutrons defines the nature of the material. The complex atomic structure is held together due to attractive forces between positive charged protons and negative charged electrons.

Niels Bohr, one of the most important scientists of the last century, proposed the *Bohr's model*, which basically states that electrons are organized in specific orbits known as shells, rounding around the nucleus. Each shell assembles the electrons by energies, being the lower ones the less energetic and the outermost, known as *valence shell*, the most energetic ones. Electrons can perform a transition on shells (from lower to higher) absorbing energy, or its counterpart by releasing energy, as it is displayed in **Figure 1.6**.

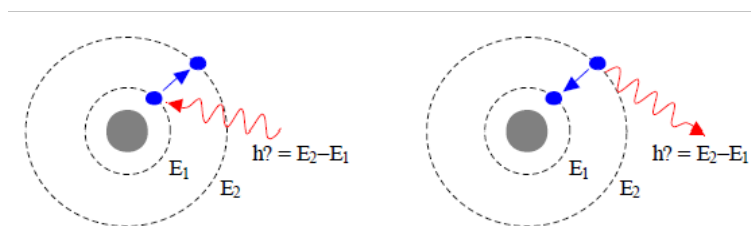


Figure 1. 6: Electron transition from lower to higher shells (left) and from higher to lower shells (right)

In order to perform a correct interpretation of the electrical behavior of each material, is very important to consider the temperature at which such material is exposed. Let us consider the case of the absolute zero (0°K); in this scenario, all the electrons are static and tightly held by their atoms, which basically means that there is no electrical conductivity. Increasing the temperature, therefore the thermal energy, the electrons acquire energies and some of them break free from the atoms. Those electrons, called *free electrons*, play a role in the electrical conductivity of a material since can flow freely.

However, there will be a point where the increase in temperature will not increase the conductivity anymore, as it is shown in **Figure 1.7**. At this point, the conductivity saturates, because of the fact that the free electrons will collide with the oscillating atoms (due to heat), reducing their speed. Therefore, the movement of the free electrons finds more obstacles and the material conductivity property saturates.

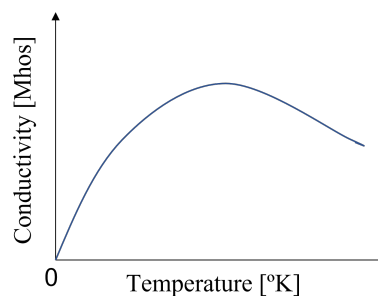


Figure 1. 7: Conductivity vs. Temperature

Another important factor to consider is the chemical stability. To reach such stability, in most of the elements, the valence shell must be filled with eight electrons, except for the first shell (with only 2 electrons) which is widely known as the *octet rule*. Each element has different amount of valence electrons, which essentially are responsible for interacting with other atoms; in cases of elements with five or more valence electrons, after reaching a chemical stability, remaining electrons can increase the negative charge of the atom. In this case, the atoms with overall negative charge are considered to be *negative ions*. On the other hand, for elements with

three or less valence electrons, there will be a *positive ions* behavior, since such electrons were able to escape, leaving the atom with an excessive positive charge. The upshot of such formation drives a formation of a bond between the positive and negative ions, known as *ionic bond*. Another kind of bond is produced when elements with four valence electrons do not receive or offer any of them, thereby *covalent bonds* are created (Michalopoulos, 2002).

In one atom, the electrons will occupy the orbitals in such a way that its energy is the minimum possible, as it was discussed previously. In order for this to occur, the orbitals are ordered according to its growing energetic level. The energy of each orbital is determined by the quantum numbers n and l , in **Figure 1.8** it is shown the orbitals of the first four levels of energy (from $n=1$ to $n=4$) and its energy order. All the orbitals of same type that exist in a energy level have the same energy (s,p or n).

Once the atoms come close together, the electronic energy of each atom is modified, and the energy levels start to group in energy bands. In those bands, electrons are either allowed or forbidden to exist. At this point, it is important to remind that the external shell and its electrons are the responsible to interact with other atoms, whereas the inner shells are the ones with more electrostatic forces with the nucleus.

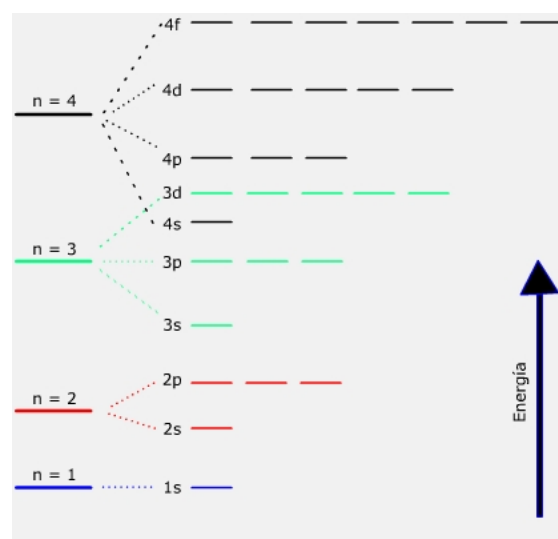


Figure 1. 8: Energy levels and orbitals.

When this external shell is fully filled, it corresponds to a state called *ground state* of the valence electrons known as valence band, this is done since the ground state provides the electronic configuration with the lowest possible energy. In this valence band, the outer electrons are bounded to the nucleus with less forces, so that those can perform bonds with another atom.

In the case where various electrons have abundant energy, it is possible for an electron to jump into a higher energetic band, known as the *conduction band*. Such electrons allow a material to conduct electricity and heat. The valence and conduction bands are separated by a *band gap*, which is the difference in energy between them. In order for an electron to cross the band gap, its energy must be higher than the band gap energy, which can vary from material to material.

To illustrate graphically the energy band diagrams, **Figure 1.9** shows how such bands are different for insulators, conductors, and semiconductors. The insulators present a valence gap mostly full and also a very high band gap ($> 3\text{eV}$), which drives to almost empty conduction band. In the other hand, the conductors present a relatively empty valence band and partially filled conduction band; in this case, there is no band gap since the valence and conduction bands are overlapped; typical examples of conductor materials are the metals.

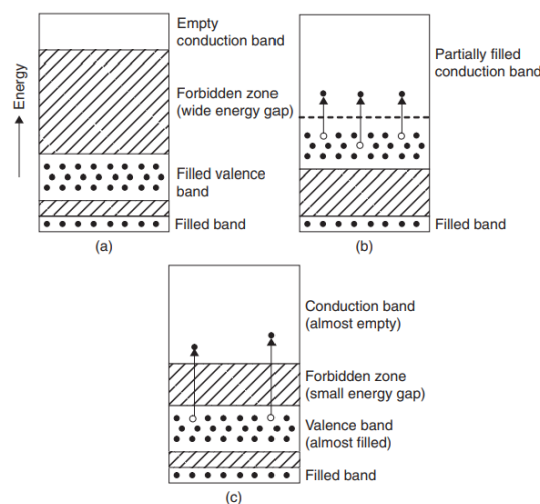


Figure 1. 9: Energy bands for typical materials. (a) Insulator. (b) Conductor. (c) Semiconductor. Adapted from (Kalogirou, 2013).

The third type of material is known as semiconductor. Its characteristics basically relies on behaving either as an insulator or conductor, depending on different external factors. Magnetic and electric field, pressure, radiation collected, temperature, are some factors that can influence on the behavior of a semiconductor. Band gap values of a semiconductor are below the 3eV (Kalogirou, 2013). Semiconductor materials are the basis of solar cell technologies, being the silicon (Si) the most common, due to its low cost and abundance on nature and the characteristic of having four valence electrons. Furthermore, there are also compound semiconductors such as Gallium Arsenide (*GaAs*) which is another material widely used on solar cells. This kind of compound elements are known as III-V materials. A variety of semiconductor (IV group) or elements which form the compounds can be seen in the periodic table of **Figure 1.10**.

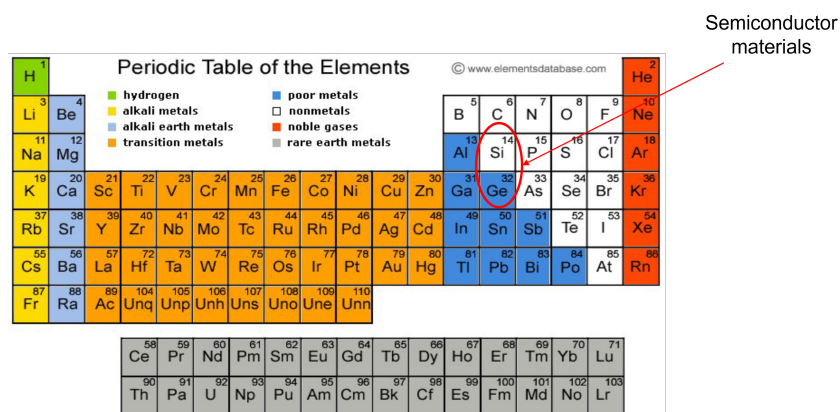


Figure 1. 10: Periodic table of elements, adapted from (Base, 2021)

1.2.2 Carriers

The two-dimensional structure of a semiconductor with four valence electrons, can be depicted as shown in **Figure 1.11**. The valence electrons interact with other electrons through covalent bonds. Moreover, the proton charge (+4) is provided in such a way that, having four valence electrons make the atom so that can be electrically charged or neutral.

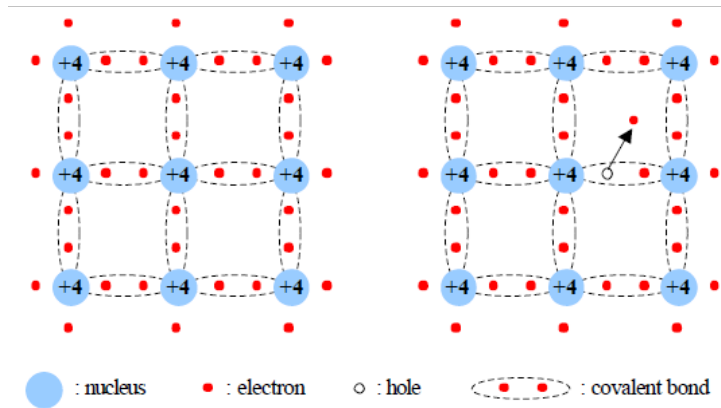


Figure 1.11: Electron disposition in a semiconductor.

However, such neutral state is not always constant, as can be seen in **Figure 1.11**, there appears something called *hole*. Once an electron acquires enough energy to jump into the conduction band, the energy of the covalent bond is overcoming and such bond breaks, driving the electron to be free. The atom loses one negative charge and since it was initially charged (+4), now there is no balance between the charges, and it becomes positively charged, where such charge is known as hole. The hole's charge is the absolute value of the electron's charge, and the position is exactly the same inside the structure as it was for the electron.

Ionization or generation, are the names for a process in which the formation of an *electron hole pair (EHP)* is done by external factors, the temperature being the most important. Such processes work also inversely, which means that it is possible for an electron to *recombine*, losing the acquired energy. The recombination phenomena are very important in the field of solar cells and will be considered in the next chapters.

The structure previously studied on **Figure 1.11**, that it does not contain foreign atoms, is known as *intrinsic* semiconductor. It is important to remark that, at absolute zero (0 K), is not possible to have generation of EHPs, but as the temperature increases, the conductivity given by the free EHP will increase too, and those generated pairs are called *intrinsic carriers*.

In order to provide a better interpretation of the growth of intrinsic carriers as a function of temperature, the three most used semiconductor materials (Ge, Si, GaAs) intrinsic carrier densities as a function of temperature are plotted in **Figure 1.12**.

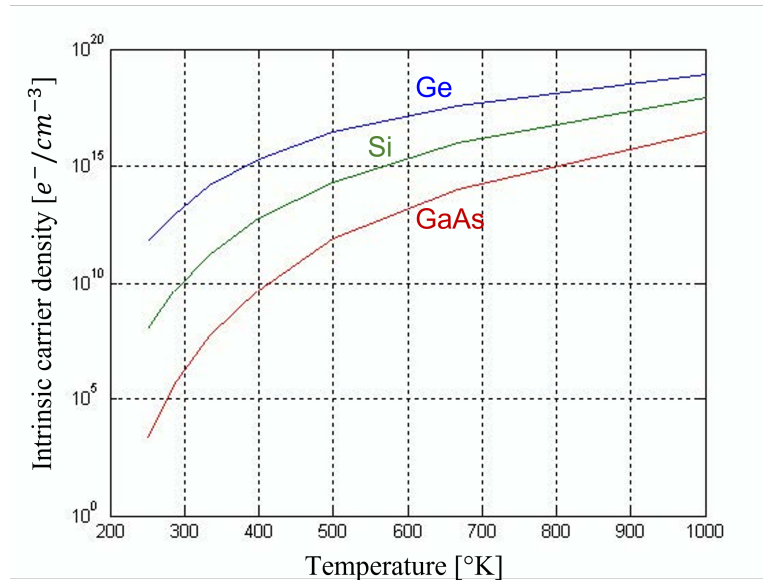


Figure 1.12: Intrinsic carrier density vs. Temperature adapted from (Michalopoulos, 2002).

To provide a scale of the very low portion of free carriers available for conduction, the intrinsic carrier concentration can be compared with the total amount of atoms in the semiconductor, as shown in **Table 1.1**.

Semiconductor	Atoms/ cm^{-3}	Intrinsic Semiconductor		
		Carrier/ cm^{-3}	Ratio	Bandgap [eV]
Ge	4.42×10^{22}	2.4×10^{13}	1: 1.8×10^9	0.66
Si	5×10^{22}	1.5×10^{10}	1: 3.4×10^{12}	1.12
GaAs	4.4×10^{22}	1.8×10^6	1: 2.5×10^{16}	1.42

Table 1.1: Carrier concentration in most common intrinsic semiconductors at 300 K, adapted from (Michalopoulos, 2002).

1.2.3 Doping

In order to increase the amount of available carriers for conduction, a process called doping has been implemented. Doping is the process of introducing impurities into an intrinsic semiconductor, which will increase the conduction of a semiconductor but also modulate its

electrical, optical, and structural properties. A doped material is known as *extrinsic semiconductor*. For instance, to obtain a doped silicon it is needed the introduction of impurities in small concentration of atoms from groups V or III of the periodic table. In the former case, given that Si possesses four available electrons to create covalent bonds, if an atom with five valence electrons is added, four of the electrons will bound but one becomes free, once again contributing to conduction; this process is called an *n-type* doping. For this type of doping, the electrons are the *majority carriers*, and the holes the *minority carriers*.

On the other hand, when an element with three valence electrons is introduced into the structure, since there is one missing electron to bound, the acceptor atom will not have enough valence electrons to share with Si atoms, so it will create a hole. This doping is known as *p-type* and present holes as majority carriers and electrons as minority ones. Both type of dopings can be observed in **Figure 1.13**.

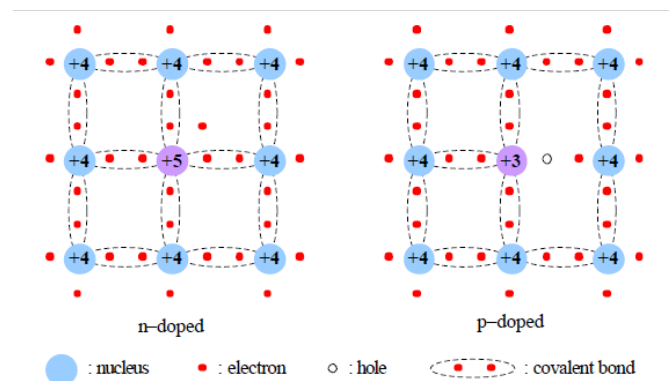


Figure 1. 13: Structures of N-type and P-type semiconductor dopings. Adapted from (Michalopoulos, 2002).

In equilibrium conditions (no bias external current applied), the product of the majority and minority is constant as it is defined by:

$$n_0 p_0 = n_i^2 \quad (1.8)$$

Where n_0 and p_0 are the electrons and holes densities respectively. The majority carrier's concentration is always equal to the addition of intrinsic and doping concentration, however since the concentration of doping is very low, the majority carrier concentration, for n-type doping, can be approximated to only the donor dopant atoms concentration:

$$n_0 = N_D \quad (1.9)$$

And p-type:

$$p_0 = \frac{n_i^2}{N_D} \quad (1.10)$$

Similarly, the majority concentration for p-type is equal to:

$$p_0 = N_A \quad (1.11)$$

And n-type:

$$n_0 = \frac{n_i^2}{N_A} \quad (1.12)$$

Where N_A is the concentration of acceptor dopant atoms. The minority carrier's concentration is inversely proportional to the doping density.

1.2.4 Fermi Level

In order to provide a complete description about the direction, concentration and energy of electrons or holes, the introduction of quantum physics is needed. In general, it is not possible to know exactly two physical observable properties, position, and physical momentum, for a given particle at the same time, this is known as *Heisenberg's principle*. Thereby, the study of probabilistic expressions was introduced.

At absolute temperature, all the electrons have energies below a specific level, known as *Fermi level* E_F . Increasing the temperature will produce the generation of electron-hole pairs, and the electrons that possess energies higher than E_F will occupy the conduction band according to the *Fermi-Dirac distribution* given in **Eq. 1.13**:

$$f(E) = \frac{1}{1 + e^{(E-E_F)/kT}} \quad (1.13)$$

Where, E is the electron energy, E_F is the Fermi level, k and T are the Boltzmann's constant and absolute temperature respectively. **Figure 1.14** shows the Fermi-Dirac distribution function at different temperatures: $T_3 > T_2 > T_1$ and $T_0 = 0K$, at $0K$ the probability of an

electron to have energies below the Fermi level is 1, and 0, for having energies higher than Fermi's (Basnet, 2015). When doping is carried out, the carrier concentrations will change, in addition to the populations on the various energy levels.

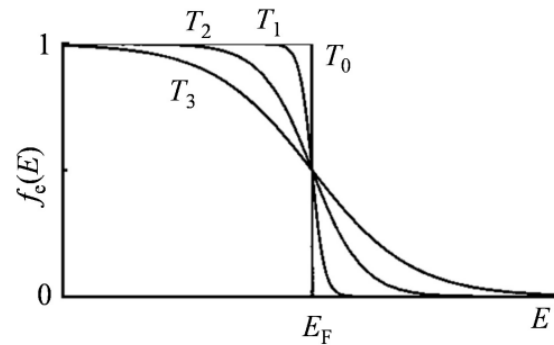


Figure 1. 14: Fermi-Dirac distribution for different temperatures (Basnet, 2015).

1.2.5 Carrier transport

A specific behavior of the carriers spreading inside a material is observable if in one side of the semiconductor exists a higher concentration of carriers. The movement of those electrical carriers will produce a current called *diffusion current* (I_D) in the direction of the less amount of carriers, as it is shown in **Figure 1.15**. Conventionally in the case of electrons as carriers, the diffusion current is in the opposite direction.

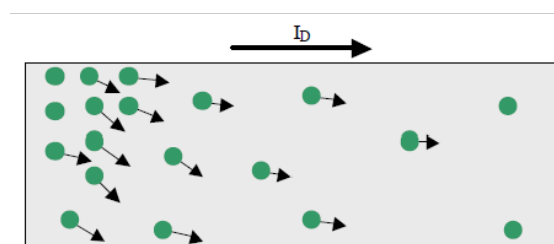


Figure 1. 15: Diffusion current produced by the movement of the carriers (Michalopoulos, 2002).

Another way to generate current can be done with the application of an external electromagnetic field. Such current is known as *drift current* (I_S), which is proportional to the intensity of the field, as it is shown in **Figure 1.16**.

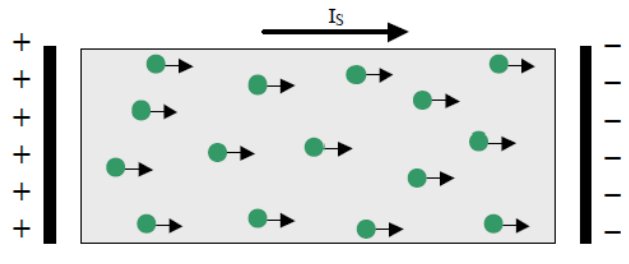


Figure 1. 16: Drift current produced by an external electromagnetic field (Michalopoulos, 2002).

The movement of the electrons eventually will reach a constant average speed known as *drift speed*. The ratio between such speed and the applied field defines a property named as *mobility* μ , which provides an information about how quickly the particle will move through a semiconductor when pulled by an electric field.

1.3 Photoelectric effect

The photoelectric effect was first proposed in 1887 by the German physicist *Heinrich Hertz*, where he observed an increase on the sensitivity of sparking by illuminating it with UV light. Then, in 1897, after the electron's discover by *J.J. Thompson*, the increment on the sensitivity was attributed to light pushing electrons (Learning, 2022).

Both definitions did not fit completely with the classical theory of electro-magnetic radiation since light was thought to behave as transversal waves. *Albert Einstein* provided a definition which helped to understand the whole effect, that is that light is composed by quanta of energy or photons.

It has already been introduced that *Planck's formula* ($E = \hbar\nu = \hbar c/\lambda$), relates the energy of the electromagnetic radiation with the frequency or wavelength of such radiation, in a way such that light propagates following linear wave equations. However, light can only be emitted and absorbed as discrete amounts.

1.3.1 The wave-particle duality

The principle of wave-particle duality expresses that matter and light exhibit particle and wave behavior and characteristics which can be only detected at an atomic scale. In this principle, light behaves as a wave having a frequency proportional to the energy of the particle. On the other side, light can also behave as a particle with energy determined by the frequency of the wave.

Additionally, by quantum mechanics, it is possible to associate a particle with a wave function $\Psi(x, t)$ such that:

$$P(x, t) = |\Psi(x, t)|^2 \quad (1.14)$$

The wave function expresses the probability of finding a particle in a point x at time t .

1.3.2 Photovoltaic effect

When light is irradiated on a metal, the surface electrons are excited and eventually released, as it is shown in **Figure 1.17**, since they acquire energy from the light and, its flux provides a current flow. In order for the photoelectric effect to occur, photons with energy high enough must interact with the surface of the metal. The photovoltaic effect is strictly related to the photoelectric effect, but in this case instead of electrons being ejected from the material, the absorbed photons will create EHP inside the material itself, creating a non-equilibrium state and carriers that, if collected externally, can generate a net amount of current.

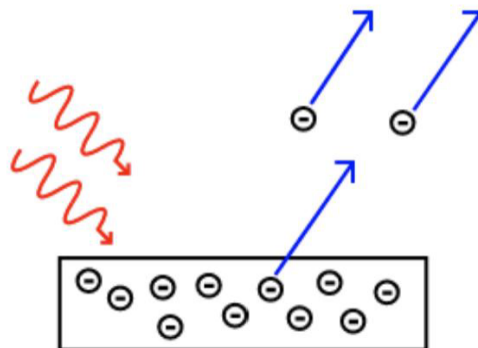


Figure 1. 17: Photoelectric effect: electrons are emitted from matter (Learning, 2022)

CHAPTER 2: SOLAR CELLS

2.1 Solar cell working principle

In the previous section it has been introduced briefly the working principle of a solar cell, which is the photovoltaic effect. The basic idea is to obtain electric energy from the abundant electromagnetic radiation produced by the sun. Previously it has been presented how the absorption of photons by a material can excite the electrons, so that a differential of potential is created, thereby this electrical energy can be collected and subsequently used as source of energy. This effect can be studied as follows:

1. Generation of charge carriers

Once the flux of photons is absorbed by a material, the absorbed energy will excite the electrons from its initial energy level E_i into a higher one E_f . **Figure 2.1** shows the absorption of a photon under following condition: in order to absorb a photon with energy $E = h\nu$, the bandgap energy of the electrons $E_g = E_c - E_v$, must be equal or lower to the incident photon energy. In such case, a hole is created, forming the electron-hole pair and so excess carriers. If the photon has less energy than the bandgap, it will not be absorbed, instead will go through the material.

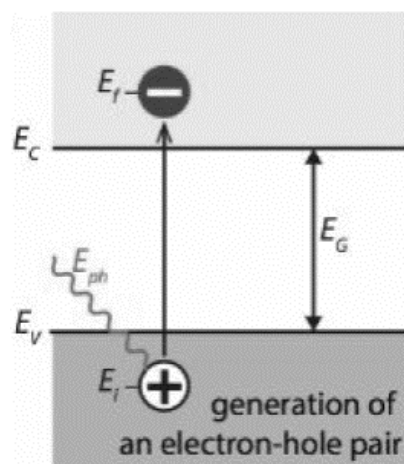


Figure 2. 1: Absorption of photons in semiconductors (a), and its posterior effect of thermalization (b). Adapted from (Smets et al. ,2015)

2. Separation of photo-generated carriers in the junction.

Figure 2.2 illustrates how charges can be pulled at the borders of the material, by introducing *semipermeable membranes* formed by n- and p- type materials, which will attract electrons to one side, and holes to the other (Würfel & Würfel, 2016). To optimize a solar cell, a condition must be fulfilled: the electrons and holes must reach the membranes before they recombine, since after a certain time, the electron-hole pairs generated will recombine releasing energy.

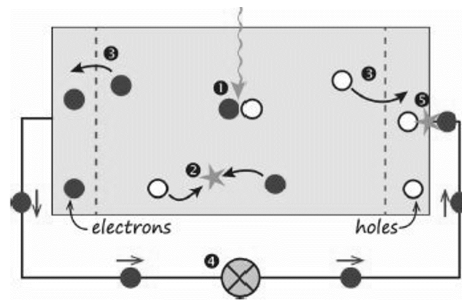


Figure 2. 2: Simple solar cell model. (Smets et al.,2015)

3. Collection of carriers at the terminals of the junction.

Once the carriers are separated, electrons will be conducted through an external electric circuit producing a flux of current. This process demonstrates how the chemical energy can be converted into electric energy through photovoltaic effect. Finally, the flux of electrons is guided to recombine with the holes that were separated to the other side.

The process shown above is present in a variety of different materials of the periodic table and their compounds. However, the most used one, due to its low-cost production and well-known behavior in electronics, is silicon. It is important to remark that the design and optimization of solar cells is strictly aligned with the final cost needed to produce electrical energy from them.

2.2 Generation and recombination

Considering a light pulse illuminating a semiconductor and a concentration of holes or electrons higher than the equilibrium concentration, so that $np > n_i^2$, meaning that there exists an

excess of carriers. When the pulse stops, such excess of electrons will recombine with holes, in order to reach equilibrium. There exist different types of recombination, which will depend on the behaviour and type of semiconductor. The negative effect of recombination is that when it occurs the collected current will be minor and part of it will be lost through undesired heat.

In order to provide a complete description of both generation and recombination, it is important to introduce the concepts of *direct* and *indirect* semiconductors. **Figure 2.3** shows the electronic dispersion diagram for direct and indirect semiconductors, where the momentum of the carrier is plotted as a function of its energetic level.

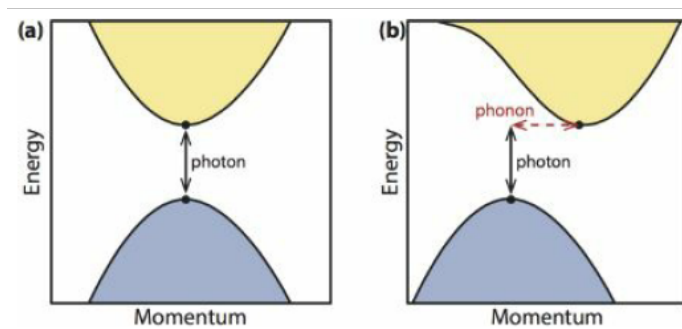


Figure 2. 3: Electronic dispersion diagram for (a) direct bandgap and (b) indirect bandgap semiconductors. (Smets et al., 2015)

To differentiate both direct and indirect semiconductors, notice that in the former case, the highest point of the valence band is fully aligned with the vertical point of the conduction band, basically the electron from the valence band will just require the energy of the photon to be excited and move to the conduction band; meanwhile, the indirect one does not present the alignment between valence and conduction highest/lowest points, which will require more energy to excite the valence electron involving a phonon, which is energy associated with the vibrations of the crystal lattice (phonons) (Smets et al., 2015).

2.2.1 Direct bandgap processes

In direct bandgap semiconductors, the generation and recombination are known as *radiative* processes. In order for a process to be radiative, one photon is absorbed when an electron-hole pair is created, and one photon is emitted when another EHP recombine directly.

Radiative generation

The radiative generation is simplified with the photogeneration process, since light will penetrate through a material breaking the bonds of the valence electrons making them to move to the conduction band, so that the electron-hole pair is created. This effect is resumed on **Figure 2.4(a)**.

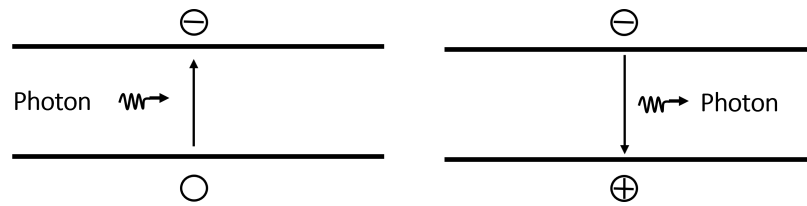


Figure 2. 4: Radiative generation (a) and recombination (b) for direct bandgap semiconductors.

In order to calculate the amount of absorbed photons in a semiconductor, a combination of the *Lambert's law* with the photon flux $\Phi(x)$ is given in **Eq. 2.1**. Where $\Phi(x_0)$ is the incident photon flux, and $\alpha(\lambda)$ is the absorption coefficient.

$$\Phi(x) = \Phi(x_0) \exp [-\alpha(\lambda)x] \quad (2.1)$$

2.2.2 Radiative recombination

The radiative recombination or also called *band-to-band recombination*, is a direct type of recombination where the excited electron comes back to its previous energy level recombining with a hole, as it is shown **Figure 2.4(b)**. As a result of the process a photon is emitted.

The radiative recombination rate (U) per unit time and volume is given as:

$$U_{\text{rad}} = B\eta p = B(n_0 + \Delta n)(p_0 + \Delta p) \quad (2.2)$$

Where B is a semiconductor proportionality factor, η and p are the total concentration of carriers, electrons, and holes respectively, n_0 and p_0 are the equilibrium concentrations (in dark), and Δn and Δp are the excess carrier concentrations given as $\Delta n = n - n_0$ for both carriers. The recombination rate measured for silicon is $9.5 \times 10^{-15} \text{ cm}^3/\text{s}$, which indicates

the low probability of this type of recombination to occur (Schlangenotto, Maeder, & Gerlach, 1974), since silicon is an indirect bandgap semiconductor.

Another important concept in recombination, is the *minority carrier lifetime* (τ), such factor expresses the time in which recombination takes place and it is used to quantify the recombination losses. First of all, let us introduce the *lifetime* statistical concept, this time represents how much time an electron passes without falling into recombination, it is expressed as: $\tau = \Delta n / U$ (Maccaronio, 2017). Then, it is possible to define the lifetime of the radiative recombination as follows:

$$\tau_{\text{rad}} = \frac{\Delta n}{B(n_0 + \Delta n)(p_0 + \Delta p)} \quad (2.3)$$

2.2.3 Auger recombination

Auger recombination is the predominant process to occur for indirect semi- conductors with high concentration of dopants. This type of recombination is similar to a direct recombination, with the difference of, in this process three particles are involved, as it is shown in **Figure 2.5**.

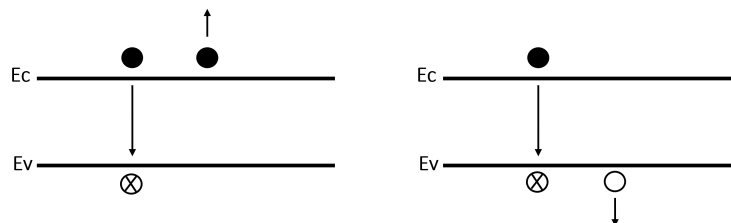


Figure 2. 5: Auger recombination with the presence of (a) two electrons; and (b) two holes.

In Auger recombination, the transition energy (momentum and energy) of the recombining carrier, is conserved by transferring it to another particle (either in valence and conduction band). The electron that receives the energy, is excited into higher levels in electronic band, will transfer its energy to vibrational energy of the lattice (phonon modes). On the other hand, if the third particle is a hole, it is excited into deeper levels of the valence band, again when it comes to its normal state it will release energy to phonon modes.

Auger recombination is mostly observed in highly doped materials (doping concentrations higher than 10^{17} cm^{-3}), and consequently is one of the most important losses in the most doped regions of solar cells (Maccaronio, 2017). The Auger recombination rate strongly depends on the charge carriers densities, and it is given as:

$$U_{Auger} = (C_n n + C_p p)(pn - n_i^2) \quad (2.4)$$

Where C_n and C_p are proportionality constants strongly dependent on the temperature. The lifetime can be expressed, either for a n-type and p-type as:

$$\tau_{Auger} = \frac{1}{C_n n_0^2} \quad (2.5)$$

2.2.4 Shockley-Read-Hall recombination

The Shockley-Read-Hall recombination is produced by the introduction of an impurity or lattice defects. Such imperfections conduct to the creation of allowed energy levels (E_T) inside the forbidden gap, known as *trap states*, which can *trap* the carriers, and after a while those can recombine with another carrier that was attracted by the first trapped carrier.

This non-radiative type of recombination, known as *SRH recombination*, due to its discovery from Shockley and Read (1952) and, Hall (1952), is predominant in majority of semiconductors, including silicon, at most common operational conditions. The phenomenon happens in a series of phases and it depends on the type of trap, that can be *donor-type*, which is positively charged and *acceptor-type*, negatively charged. **Figure 2.6** shows the steps of the process of SRH recombination:

- S1: An electron is trapped from the conduction band.
- S2: An electron is emitted from the trap state, again to the conduction band.
- S3: A hole is trapped from the valence band.
- S4: A hole is emitted from the trap state to the valence band.

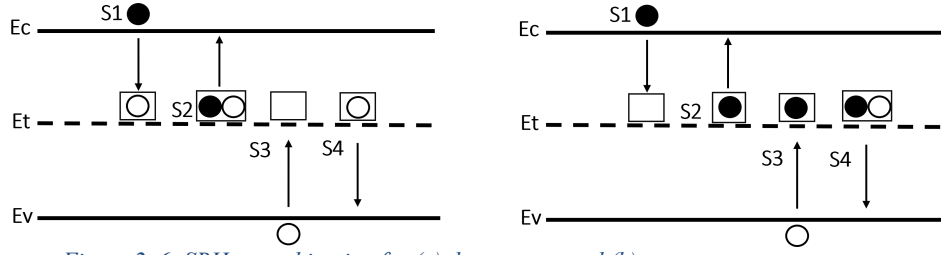


Figure 2. 6: SRH recombination for (a) donor-type; and (b) acceptor-type traps.

In order to get the recombination rate of SRH recombination, is needed the calculation of the probabilities of each event to occur. This rate is given by:

$$U_{\text{SRH}} = V_{TH} N_t \frac{(np - ni^2)}{\left(\frac{1}{\sigma_p}\right)(n + n_1) + \left(\frac{1}{\sigma_n}\right)(p + p_1)} \quad (2.6)$$

Where V_{TH} is the thermal velocity (average velocity of electrons and holes due to thermal movement), N_T is the density of traps, σ_n and σ_p are the capture cross section for electrons and holes respectively (effectiveness of the trap state to capture a carrier), the variable n_1 and p_1 are:

$$n_1 = n_i \frac{E_t - E_i}{kT} \quad (2.7)$$

And,

$$p_1 = n_i \frac{E_i - E_t}{kT} \quad (2.8)$$

Being, E_t the energy level of the defect. The SRH lifetime is given in **Eq.2.9**. Notice that the lifetime is inversely proportional to the capture cross section, high temperatures and trap densities.

$$\tau_{\text{SRH}} = \frac{1}{\sigma V_{TH} N_T} \quad (2.9)$$

2.2.5 Surface Recombination

Surface recombination, as the name predicts, is a type of recombination that occurs at the surface of a semiconductor, in contrast to the other type of recombination that occur in bulk. Since there are always electrons that do not bond with any element, they create defects at the

surfaces or interfaces between different materials. Thereby, the defects create surface trap states in the bandgap that will induce SRH recombination. Most of the pure semiconductors present surface recombination as one of the most influential recombination effects. The surface recombination rate for n-type semiconductor, is expressed by:

$$U_S = V_{TH} \sigma_p N_{ST} (p_s - p_0) \quad (2.10)$$

Where V_{TH} is the thermal velocity, N_{ST} is the surface trap density given in cm^{-2} , p_s is the hole concentration at the surface and, p_0 is the equilibrium hole concentration in the semiconductor. An important factor in the design and optimization of solar cells is the parameter called *surface recombination velocity* (see **Eq.2.11**), which should be kept as low as possible to reduce losses of carrier at the surfaces. There exists two ways to reduce this value, the first one is trying to reduce the trap density N_{ST} by a technique called *passivation*, where a layer of a suitable material is deposited onto the semiconductor surface. In the second case, it is possible to reduce the minority carrier concentration at the surface, by doping the region underneath to introduce a surface field that create *shells* (Smets, 2015).

$$S_r = V_{TH} \sigma N_{ST} \quad (2.11)$$

2.3 Parameters of a solar cell

2.3.1 I-V characteristic

The solar cells performance is evaluated on different output figures of merit. One of the most fundamental analysis of solar cells comes from the obtained *IV curve* derived from a *p-n junction*, shown in **Figure 2.7**. In such graph, it is possible to observe that the illuminated curve can be obtained by a rigid downward shift, which is equal to the photogenerated current I_L .

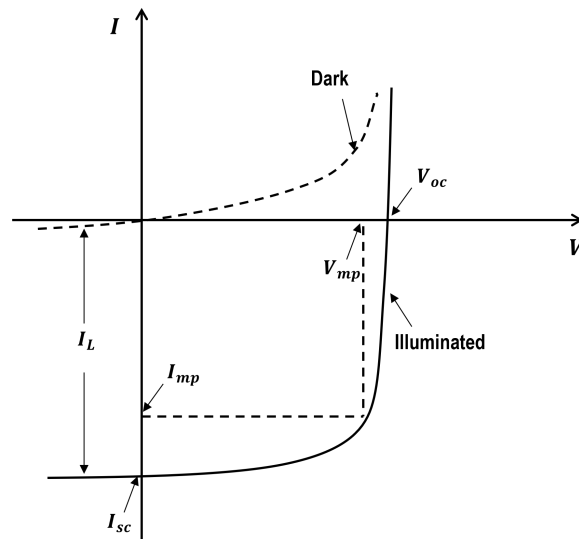


Figure 2. 7: I - V characteristic of a solar cell under dark and illuminated conditions.

The relation between the voltage and the total current is obtained through an analysis of the p-n junction (see detailed demonstration on *Green's* publication (1982)). Equations 2.12 and 2.13 represent the current relation for dark and illuminated curves respectively. The remaining parameters will be detailed in the next sections.

$$I = I_0 \left(\exp\left(\frac{qV}{kT}\right) - 1 \right) \quad (2.12)$$

$$I = I_0 \left(\exp\left(\frac{qV}{kT}\right) - 1 \right) - I_L \quad (2.13)$$

Saturation Current I_0

The saturation current parameter has a strong relation with the semiconductor properties. Regarding the design of solar cells, such current must be kept as low as possible, which requires good fabrications techniques and processes. The Shockley expression (Shockley W. , *The Theory of p-n Junctions in Semiconductors and p-n Junction Transistors*, 1949) for the saturation current is:

$$I_0 = A \exp\left(-\frac{E_G}{kT}\right) \quad (2.14)$$

where A , is a material dependent constant, found to be $2.25 \times 10^5 A$ (Ravindra & Prasad, 1980) per unit area 1cm^2 , and E_G is the energy bandgap of the semiconductor.

Photogenerated Current J_{ph}

The photogenerated current in a semiconductor depends on the collection of photo-generated carriers. This factor appears only in illuminated IV characteristics since in dark it will be zero. Usually, photogenerated current is expressed in terms of density to normalize with respect to the cell area, so that $J_L = I_L/A$, where A is the illuminated area of the solar cell.

Figure 2.8 shows the maximum photogenerated current density that a solar cell with different materials can produce, the solar spectrum used for such comparison is the AM1.5, notice that one of the best responses of generated photocurrent is given by a crystal silicon.

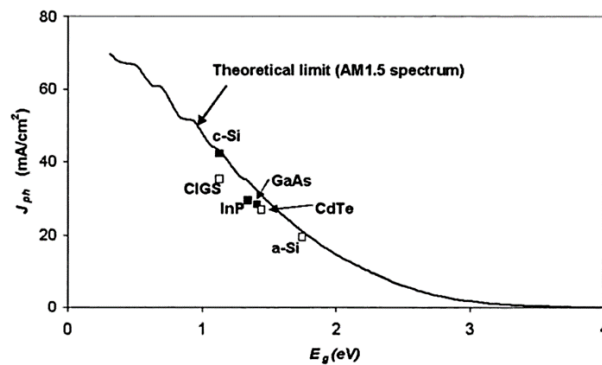


Figure 2. 8: Theoretical limit on photogenerated current in comparison with the best measured values, at AM1.5 photon flux (McEvoy & Markvart, 2003)

2.3.2 Short-circuit current I_{SC}

When the cell is under illumination and in a short-circuit condition, the maximum current possible is generated. Working on ideal conditions, the I_{SC} is approximately equal to I_L . The short-circuit current depend on the incident photon flux, optical losses that occur before reaching the p-n junction, and the area of the cell, in this latter case the dependency of the area can be suppressed by working on terms of the short-circuit current density J_{SC} . Making a similar

analysis for this current, with the photogenerated one, the crystalline silicon (c-si) in AM1.5 spectrum, can provide a maximum of $J_{SC} \leq 46mA/cm^2$.

2.3.3 Open circuit voltage V_{OC}

The open-circuit voltage is the voltage at which no current flows through the external circuit (Smets, et al., 2015). Such voltage defines the maximum voltage that the solar cell can produce and to obtain the expression for the V_{OC} , the total current I has to be zero. Inserting this condition in **Eq.2.13**, we obtain:

$$V_{OC} = \frac{kT}{q} \ln \left(\frac{I_L}{I_0} + 1 \right) \quad (2.15)$$

Notice the dependence of the open-circuit voltage with both the photogenerated and saturation currents. While the I_L has small variation, the I_0 , as it was defined, will vary according to the material behavior, thereby the material will also define the recombination capability of the solar cell. The V_{OC} is then strongly affected by the recombination effects. The c-si solar cells under AM1.5 spectrum has values of $V_{OC} \leq 720mV$.

2.3.4 Fill Factor

The concept of fill factor can be explained observing **Figure 2.7**. There are *squared* points as I_{mp} and V_{mp} , which indicates the maximum possible output power, known as the maximum power point (MPP). The ratio between the MPP over the product $V_{OC}I_{SC}$ gives the fill factor FF , that is a measure of how *squared* the output characteristic is. FF is defined as:

$$FF = \frac{V_{mp}I_{mp}}{V_{oc}I_{sc}} \quad (2.16)$$

For cells with a reasonably efficiency, the FF value ranges between 0.7 and 0.85, 1 being the maximum and ideal case. In such case, where the cell behaves as an ideal diode, the fill factor can be approximated in terms just of the V_{oc} (Green M. A., 1982) as follows:

$$FF = \frac{v_{oc} - \ln(v_{oc}) + 0.72}{v_{oc} + 1} \quad (2.17)$$

Where $v_{oc} = V_{oc}(q/K_B T)$, is the normalized voltage. Graphically, the FF can represent the "squareness" of the solar cell and is also the area of the largest rectangle which will fit in the IV curve, as it is depicted in **Figure 2.9**.

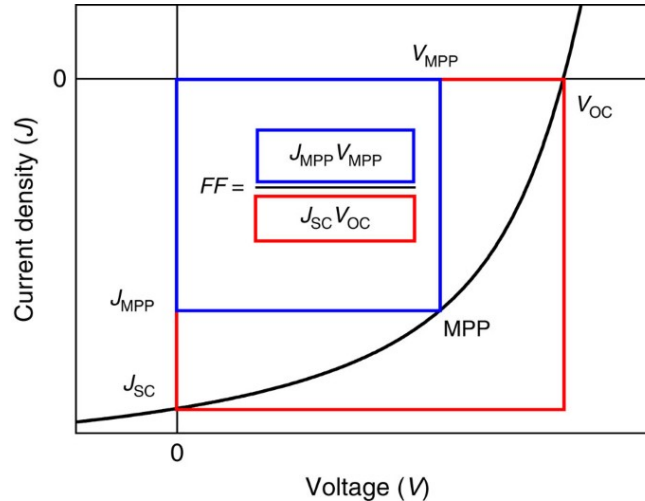


Figure 2. 9: Fill factor represented in the IV characteristic curve (Bartasaghi, et al., 2015)

2.3.5 Energy-conversion efficiency

The efficiency of a solar cell η is defined on how much incident power is converted into energy, and it is possible to calculate it, as the ratio of the maximum power generated and the incident power:

$$\eta = \frac{P_{Max}}{I_{in}} = \frac{I_{mp} V_{mp}}{I_{in}} = \frac{I_{sc} V_{oc} FF}{I_{in}} \quad (2.18)$$

The efficiency reported on the market for single-junction solar cells are in the order of 17-18% for normal (medium) quality. This value increases to 20% for high quality solar cells. The efficiency value can improve depending on the configuration and materials of solar cells, however, it cannot exceed the limit of *Shockley and Queisser* (1961). Which states that one single-junction silicon solar cell cannot exceed a conversion efficiency of 30-35% as it is plotted in **Figure 2.10**.

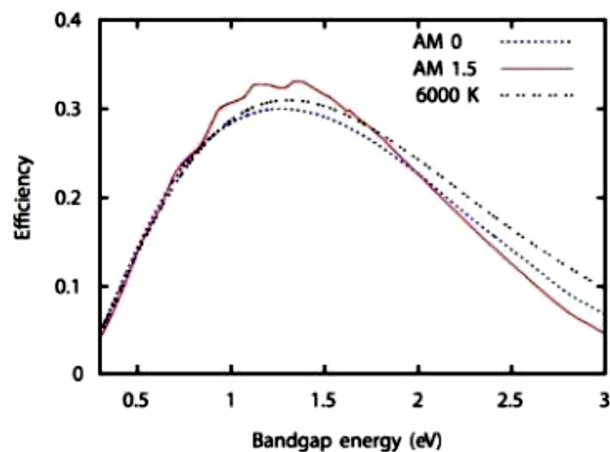


Figure 2. 10: Efficiency Shockley-Queisser limit. Adapted from (Smets, et al., 2015)

2.4 Progress and performance of solar cells

2.4.1 Single-crystalline cells

Most of the commercial solar cells are silicon-based cells (c-Si); the first implementation was in 1954 at *Bell Laboratories*, this is considered the foundation of the solar cell technology, and it had an efficiency of around 6% (Chapin, Fuller, & Pearson, 1954). Over time, the structures of such c-Si cells have been modified to increase the power efficiency conversion, with the implementations of different techniques such as the use of an antireflective layer at the top of the cell, to reduce the amount of light lost to reflections. In this same direction, the use of a textured pyramidal shape was also introduced at the top of the cell in order to enhance a better absorption of light, and finally to avoid surface recombination passivation layers were also included. With the improvements given by those modifications, the solar cell (usually refereed as *PERL* cell, see in **Figure 2.11 a**) reached a maximum of power conversion energy (PCE, which is the ratio between incident photon energy over the electrical energy output) of 25%. Nevertheless, the major drawback of this architecture is the loss in the photogenerated current, due to shadowing created by the grid contacts and also surface recombination created at to same contacts.

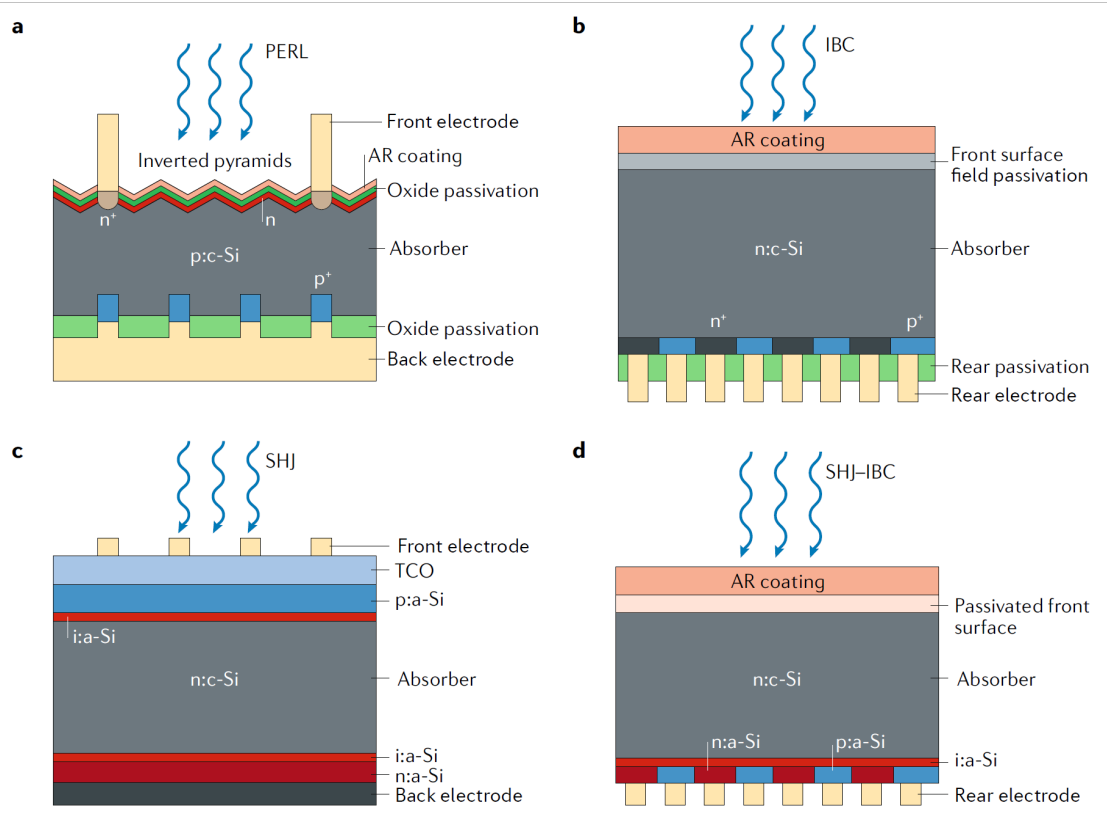


Figure 2. 11: Device architectures of different types of c-Si single cells. Adapted from (Nayak, Mahesh, Snaith, & Cahen, 2019)

The interdigitated back contact (IBC, see **Figure 2.11 b**)) configuration was proposed to address the main problems of the *PERL* cell. It reduces the shading since there is not a top grid, having instead both contacts on the back side, and also the optical behavior is improved given the possibility to design the top surface for optimal light trapping.

The other issue of *PERL* cell, the recombination at the contact surfaces, was decreased introducing a Si hetero junction (SHJ, see **Figure 2.11 c**)). The working principle of the SHJ is basically placing a thin layer (intrinsic hydrogenated amorphous Si, in this case) between the absorber (c-Si) and both the n-doped or p-doped contacts to decouple passivation from charge collection. Notice the addition of a TCO (Transparent conductive oxide) layer underneath the front electrodes, whose concept will be extended in next chapter. Taking in consideration both of the advantages from SHJ and IBC cells, a different configuration was also proposed (SHJ-IBC, see **Figure 2.11 d**)), in which it was possible to obtain a PCE of around 26.7%.

GaAs, GaInP, InP cells

Another material widely used in solar cells is the Gallium Arsenide (GaAs, see **Figure 2.12 a**)), which is a III-V compound material with very interesting optical properties such as a higher bandgap than silicon, best suited to absorb high energetic photons. Architectures using GaAs have reported a maximum PCE of around 29.1 % (Kayes, et al., 2011). In the design of high-performance cells, the GaAs thin film cells generally are more suitable to the use of highly reflective back contacts instead of substrates (to reduce parasitic absorbance).

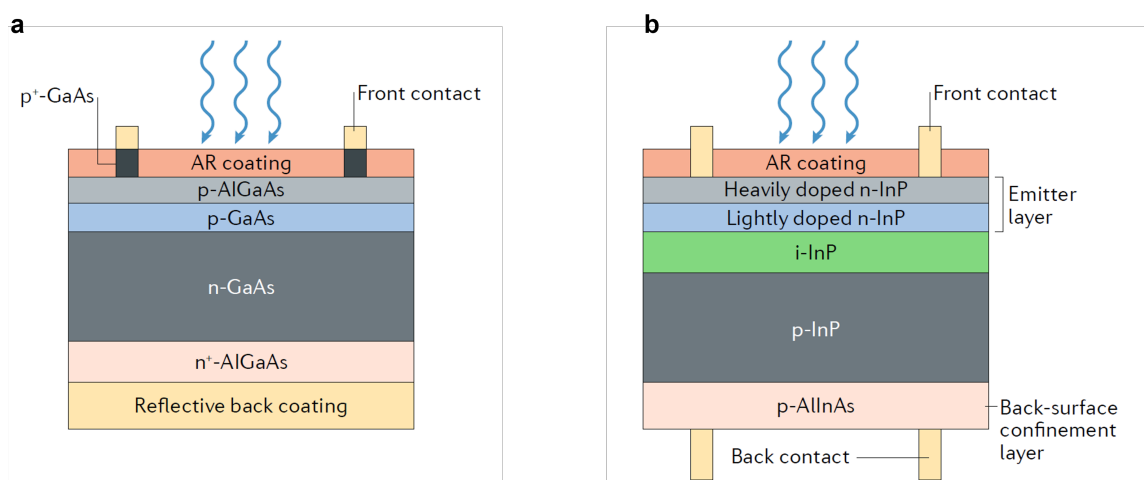


Figure 2. 12: Device architectures of different types of GaAs cells. Adapted from (Nayak, Mahesh, Snaith, & Cahen, 2019)

The *GaInP*-based solar cells are also a category of cells, in which GaAs can be a substrate in an upright configuration with a gold back reflector, in which the maximum values of PCE are around 20.8%, or by tuning the chemical configuration of Ga:In ratio, the PCE can reaches 24.4% (Nayak, et al., 2019).

The Indium Posphide (InP, see **Figure 2.12 b**)) crystalline cell also shows PCE of approximately 24.2%. The interesting characteristic in this case is that the increase of photocurrent efficiency is achieved using a high-low doping technique in the emitter layer (Nayak, et al., 2019).

Multi-junction solar cells (Tandem)

In the previous sections, it has been presented the most predominant technology on photovoltaic, which is the single-junction solar cells. The huge impact on the market for this type of cells relies mostly on the low production cost but still good overall performance. However, this type of cells has reached its efficiency limit around 30%. In this scenario, the attempts to improve the maximum efficiencies increased, always keeping in consideration the trade-off between low-cost fabrication and energy production capabilities.

From this consideration the research efforts were also dedicated to a multi- junction architecture development. In principle a multi-junction cell, or known as *tandem cell*, is composed by a stack of various absorbing semiconductors characterized by different bandgaps. The idea behind the multiple absorbers is to optimize each layer to absorb a portion of the solar spectrum, as it is shown in **Figure 2.13**. Instead of using one junction for the whole spectrum, the multi-junction cell performs the energy conversion by levels. The efficiency of this design can grow until a theoretical limit of around 46% (Bailie, 2015).

Regarding the design of a tandem cell, a large bandgap solar cell is located at the top of the cell and will absorb the high-energy portion of the spectrum to extract the current at high voltages. Such device is transparent to the lower section of the spectrum, so a new solar cell designed to absorb such spectrum must be located beneath, and thereby extract the current at low voltages.

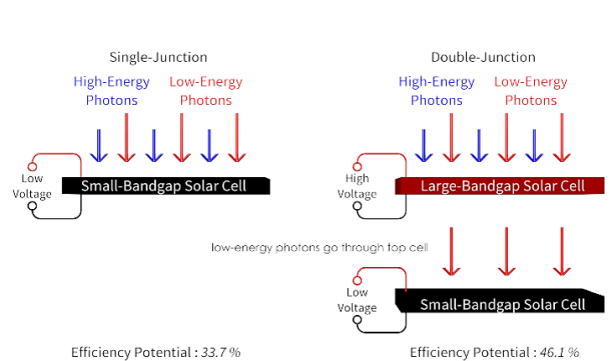


Figure 2. 13: Efficiency comparison between a single-junction and double- junction solar cells. Adapted from (Bailie, 2015)

Tandem architectures

Two ways of designing tandem solar cells have been developed: mechanically stacked and monolithically integrated (see **Figure 2.14**). The first type combines two different fabricated solar cells organizing them one on top of the other. The production and optimization can be done independently, which eliminates some of the restrictions (e.g. no recombination layer required). The second type is the classic structure used in the majority of III-V tandems and organic tandem design. In this monolithic structure the junctions are deposited one on top of the other, which creates a single solar cell with only two contacts. In order to achieve this last design, a tunnel junction or recombination layer must be created between each junction, so that current can flow between junctions. Like the first architecture, the monolithic one present drawbacks, the most prominent is that the current that pass through the junctions must be matched.

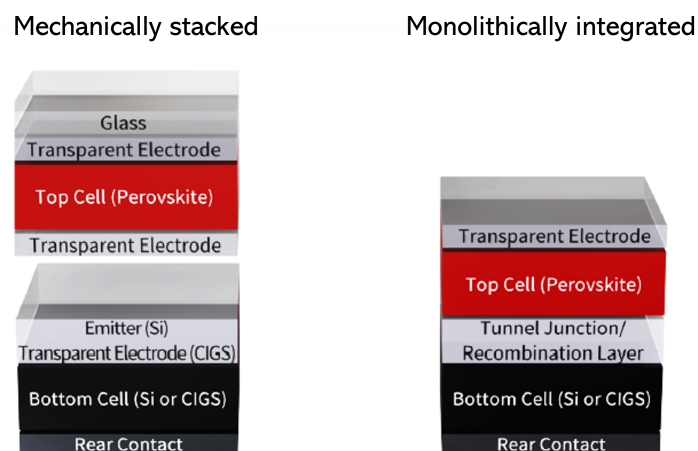


Figure 2. 14: Scalable tandem architectures. Adapted from (Bailie, 2015)

In order to best choose the materials for the junctions, it is important to consider the specific bandgaps and how they can be combined to absorb in the most ideal way the larger portion of the light spectrum. In this regard the tandem architecture offers much more versatility and optimization room with respect to a single junction cell. To design the best possible combination for a tandem cell in standard conditions AM1.5 the absorber bandgap for the bottom cell should be around 1.7-1.8 eV for the top cell and 1.1 eV for the bottom cell (Bremner,

Levy, & Honsberg, 2008), so the silicon commercial cell will work perfectly in such architecture.

2T, 3T and 4T configurations

There exists different configuration for the tandem cells according to the number of terminals. The most used ones are the two-terminal (2T) and four-terminal (4T). **Figure 2.15** presents the different configuration for tandem cells according to its terminal numbers and, number of transparent conductive electrodes (TCEs) which will be further explained later.

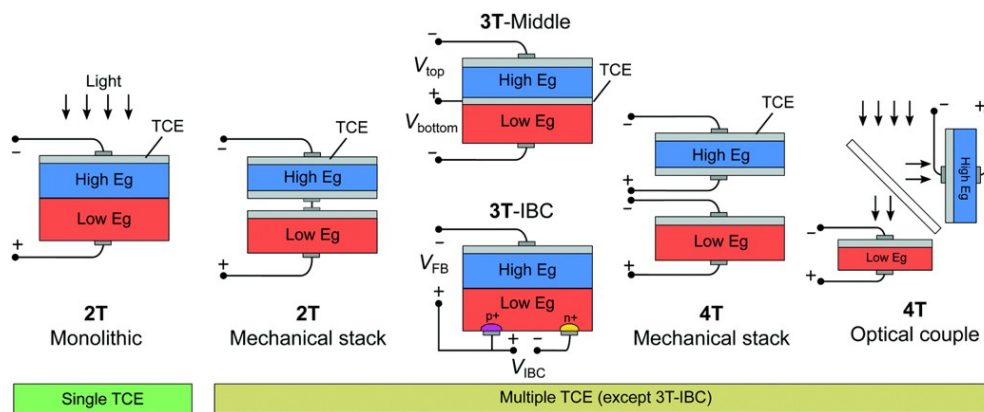


Figure 2. 15: Different multijunction configurations, organized by the number of electrical terminals. Adapted from (Martinho, 2021)

2T tandem

The most basic tandem configuration is the two-terminals monolithic tandem, it present both high and low bandgap absorber placed one on top of the other (see Single TCE on **Figure 2.15**). The limitation of this configuration is the matching current condition, since the sub cell with less bandgap energy will generate lower current but having the cell in series configuration this will limit the overall current of the cell.

On the other hand, the two-terminals mechanical stacked cell has the two cells separated and connected in series (see Multiple TCE on **Figure 2.15**). So that, the limitation of matching current is corrected by modifying the areas. Nevertheless, the optical losses increase in such configuration.

3T tandem

There are two different configurations of three-terminal tandem cells. The first one is known as the 3T-Middle tandem, in which an additional electrode is placed in the middle of the top and bottom cells, such that no series connection is needed. Since the cell has three independent terminals, this behavior is like a transistor. When top and bottom terminals are connected to different loads, the matching current can be quite relaxed. Whereas, if those terminals are connected together outside the cell, there will exist a parallel connection. The negative effect on such configuration is the limited active area due to the introduction of exposed electrodes.

4T tandem

There are two configurations for the four terminal cell architecture. The first is the 4T mechanical stacked, in which two extra terminals are introduced at the bottom of the first cell and the top of the other one. The completely electrical separation of the cells offers the advantage of the possibility of independent electrical optimization, at the cost of more shadowing due to the intermediate contact grids needed to collect the carriers. This configuration can also be reduced to 2T if the cells are connected in series, but this will again present the drawback of the matching currents, so the completely electrically separated 4T cell is the most promising and studied configuration.

The second approach is related to the use of an optical coupling that belongs to a non-monolithic system. A *dichroic filter* is used to split the solar spectrum, in such a way that the higher wavelengths are received for low bandgap absorbers and vice-versa with the low wavelengths. The negative effects of those cells are the cost of the optical system, extra wiring and difficulty to implement it.

In the majority of tandem structures, as well as some of the single-junction solar cells, one or more layers of TCO (transparent conductive oxide) were introduced and implemented

during the years. This layer is crucial in photovoltaic devices since, especially in structures with multiple contacts, it can greatly reduce the losses due to the shadowing created by the metal grids but has been also used as an electrical optimization layer given the possibility to ease the conduction by spreading the contact resistance. Since the discovery of electrical conductivity in metal oxides, the study, and optimizations of TCOs have acquired a huge interest both in research and industry (Fortunato, Ginley, Hosono, & Paine, 2007).

CHAPTER 3: TRANSPARENT CONDUCTIVE OXIDES

Transparent conductive materials, including transparent conductive oxides (TCOs), are interesting materials that exhibit high electronic conductivity and high optical transparency inside the visible light spectrum. Such combination of properties is usually impossible to find in nature, and for example, glass and silver are a simple but clear manifestation of this; in the first case the material is very transparent but also highly insulating, whereas in the second case is highly conductive but opaque to visible light. A type of material that can achieve such behavior could be semiconductors with wide bandgap.

The first co-presence of both electrical conductivity and transparency was observed in 1907 in the material called cadmium oxide (CdO). It was not well-studied until 1940, since electronic applications were on-demand day after day. Later, in 1956, transparency and conduction were found in indium oxide (In_2O_3). In the evolution of the studies on the subject, the material that has acquired wide interest is SnO_2 doped with In_2O_3 , known as indium tin oxide or ITO, due to its excellent electrical and optical properties and the superior trade-off between both with respect to other types of TCO.

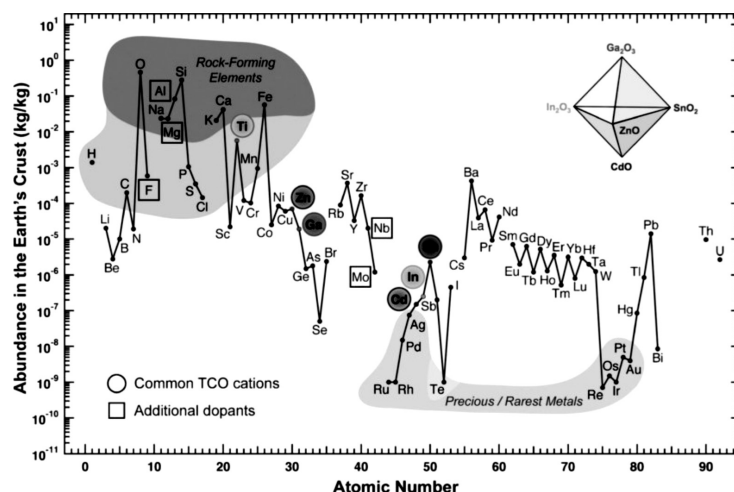


Figure 3. 1: Mass fraction abundance of the elements in the Earth's crust as a function of atomic number. Common TCO cations are highlighted by colored circles and additional dopants by squares. Adapted from (Kalowekamo & Baker, 2009)

Most of the TCOs materials behaves like degenerate n-type semiconductors, but p-type-like TCO can also be created. The most used TCOs semi- conductors are impurity-doped materials (ZnO , In_2O_3 , SnO_2 among others) as it is shown in **Figure 3.1**. The majority of those TCO materials have a wide bandgap larger than 3.0 eV and the ability to change it by doping them.

3.1 Indium-Tin Oxide (ITO)

Indium-tin oxide (ITO) or *tin doped indium oxide*, is one of the most widely used transparent conductive oxides, and its properties are high optical transmittance in the visible region, high electrical conductivity, surface uniformity, and process compatibility (Lien, 2010). ITO is comprised of three elements: indium, tin, and oxygen with a composition of approximately 90wt% of In_2O_3 and 10wt% SnO_2 .

Electrical properties of ITO

The electrical conductivity of most materials depends on two factors: the concentration of free carriers (N) and the mobility of those free carriers (μ) expressed as:

$$\sigma = N\mu e = \frac{1}{\rho} \quad (3.1)$$

where σ is the electrical conductivity, e is the electrical charge, and ρ is the resistivity of the material. It is possible to observe that the electrical conductivity presents direct proportionality with both N and μ quantities, so that, in order to increase the electrical properties, those quantities also must increase. In order to increase the free carrier concentration N , a doping process is needed. It has been reported that the electrical conductivity of ITO reaches a maximum at approximately 6-10% of tin doping, as it is shown in **Figure 3.2**. Another way to increase the conductivity is by increasing mobility, however, this depends on intrinsic scattering mechanisms, and cannot be controlled directly.

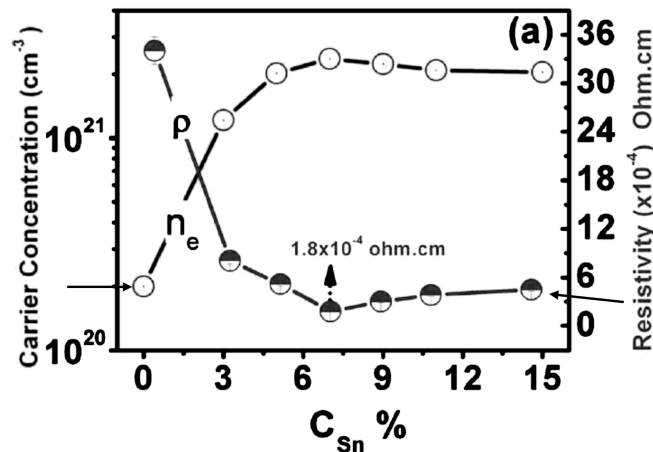


Figure 3. 2: Electrical resistivity and carrier concentration of ITO at different tin concentration (wt%). Adapted from (Mryasov & Freeman, 2001)

In order for the TCO to be used in solar cells, the presence of a bandgap with low absorption in the visible spectrum is needed. With a bandgap of at least 3eV, metal-oxide semiconductors are well suited to this application. The conduction band in this case is formed by a single dispersed metal s band, while the valence band is mostly due to the oxygen $2p$ bands.

Materials that belong to *intrinsic stoichiometric oxides*, which have elemental composition that can be divided into exact proportions, do not present the coexistence of electrical conductivity and transparency. Nevertheless, substitutional doping by cationic donors or anion vacancies can create electric carriers. After such doping, the donor (acceptor) states will alter the electronic band structure of the material. Once the donor density is increased, its states will be bound with the conduction band at a certain critical density n_c , whose value can be approximated using *Mott's criterion* (Dekkers, 2007).

$$n_c^{1/3} \cdot a_0^* \approx 0.25 \quad (3.2)$$

Where a_0^* is the effective Bohr radius given by:

$$a_0^* = \frac{h^2 \epsilon_0 \epsilon^m}{\pi e^2 m_c^*} \quad (3.3)$$

Where $\epsilon^m = 8.9$ is the dielectric constant of the host lattice for In_2O_3 according to (Hamberg & Granqvist, 1986), and $m_c^* = 0.35 \cdot m_e$, is the effective mass of the electrons in

the conduction band in terms of the electron rest mass (Köstlin, Jost, & Lems, 1975). Using these quantities, it is possible to obtain the Bohr radius $a_0^* = 1.3nm$ and the critical density $n_c = 6.4 \times 10^{18} cm^{-3}$. Notice that, in general, the carrier density for ITO, for example, reaches $\times 10^{21} cm^{-3}$, which states that above Mott critical density, the electrons will behave as free electrons. Furthermore, once the donor states are bounded with the conduction band ones, the material is said to be degenerate. So, they start to behave like semiconductors with good conductivity properties.

As stated before conductivity depends on mobility, which can be expressed as:

$$\mu = \frac{e \cdot \tau}{m^*} = \frac{e \cdot \lambda_{mfp}}{m^* \cdot V_F} \quad (3.4)$$

Where τ is the relaxation time, that depends on the λ_{mfp} mean free path and V_F drift velocity. These two parameters depend on different scattering mechanisms (lattice scattering, ionized impurity scattering, neutral impurity scattering, e-e scattering, e-impurity scattering, and grain boundary scattering). In general, the total mobility is given as:

$$\frac{1}{\mu_{tot}} = \sum_i \frac{1}{\mu_i} \quad (3.5)$$

This indicates the contribution of each type of mobility to the total, making each effect either reduce or increase the total value, which ends up in an increase or decrease in conductivity.

Optical properties of ITO

To analyze the optical properties of ITO, let's first observe the band structures of pure indium oxide and ITO in **Figure 3.3**. Indium oxide behaves as transparent in the range of visible light (400-700nm) since its bandgap has been found to be approximately 2.9 eV. According to the energy of a photon $E = hc/\lambda$, the photons with $\lambda < 427nm$ can have energies larger than

the 2.9 eV, whereas photons with $\lambda > 427\text{nm}$ have energy lower than the bandgap, so they could not be absorbed.

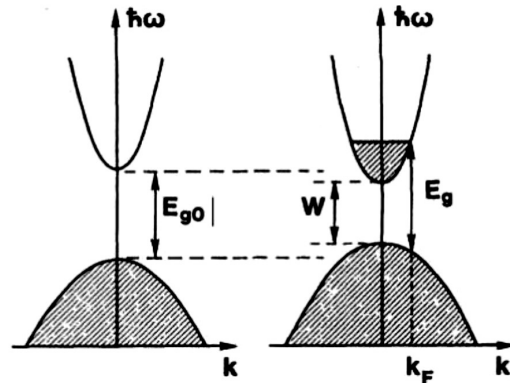


Figure 3. 3: Simplified band structures of pure indium oxide In_2O_3 (left) and ITO (right). Adapted from (Gupta, A., & Srivastava, 1989)

In contrast, the bandgap (W in the figure) for intrinsic ITO is lower, and it can decrease according to the tin doping. Moreover, the effective indirect band gap (E_g) will increase since the conduction band is partially filled. Such band gap is large enough to prevent the inter-band transitions, which ends up with an ITO transparency inside the visible range.

Then, it is possible to state that ITO can act as a dual behavioral material. A dielectric behavior inside the visible spectrum, transmitting the incoming light through it. And, a metallic behavior, in the near-infrared spectrum, possessing conductivity close to that of a metal. Thus, as the wavelength is increased there is a shift in the behavior of the material, as can be seen in **Figure 3.4**. Graphically, the point of shift occurs when the k value overcomes the n values, analyzing the optical behavior of ITO provided by (Woollam, McGaham, & Johs, 1994).

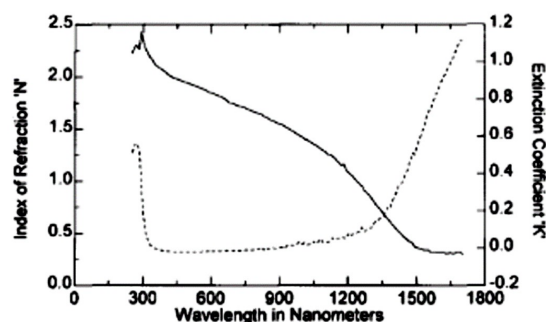


Figure 3. 4: Optical constants n (solid line) and k (dotted line) of ITO. Obtained from (Gupta, A., & Srivastava, 1989)

Correlation of optical and electrical properties

Both behaviors already studied, the optical and electrical, are interdependent on each other since their parameters are related. The plasma frequency, which is the frequency above which the real part of the dielectric function becomes positive, and the metal starts to behave like a dielectric, is affected by both optical and electrical parameters. The plasma frequency is defined as:

$$\omega_p = \frac{n \cdot e^2}{\epsilon_0 \epsilon_\infty m_c^*} \quad (3.6)$$

At a frequency in which the dielectric behavior is the same as the metallic one, the transmittance will be equal to the reflectance. Thereby, the reflectivity of the material can be tuned, ITO reflectivity can be tuned from $1.5\mu m$ to $4\mu m$, due to the carrier concentration, caused by a change in the composition and deposition parameters.

3.2 Transparent electrodes: conventional TCO films

Nowadays, the use of TCOs covers fields such as optoelectronic devices, energy-efficient windows, flat panel displays, and photovoltaic cells. The use of TCO is normally as a thin layer that can be deposited by techniques as Physical Vapor Deposition (PVD, similar to chemical one, CVD) Magnetron Sputtering (MS), or Pulsed Laser Deposition (PLD). All different techniques look for an approach that aim to decrease the resistivity while obtaining a big transmittance (around of 80-90%). Regarding the ITO films, the resistivity margin is around $10-4\Omega cm$, and sheet resistances around $10\Omega/\square$.

Different materials can be used to create a transparent conductive oxide so the specific type is chosen based on their proposed applications. ITO is a widely used material in most of the architectures of solar cells, but depending on the type of cell, other TCOs can be used, as it is shown in **Figure 3.5**. Notice in that overview, that there exists a big variety of architectures and materials using different TCOs (as organic ones, copper indium gallium selenide solar cell,

and so on). This is due to the general purpose of this TCO layer, which is to maximize the light absorption by the active layer, and in the example of the cadmium telluride (CdTe) the absorption properties of the active layer must match the NIR transmittance of the TCO.

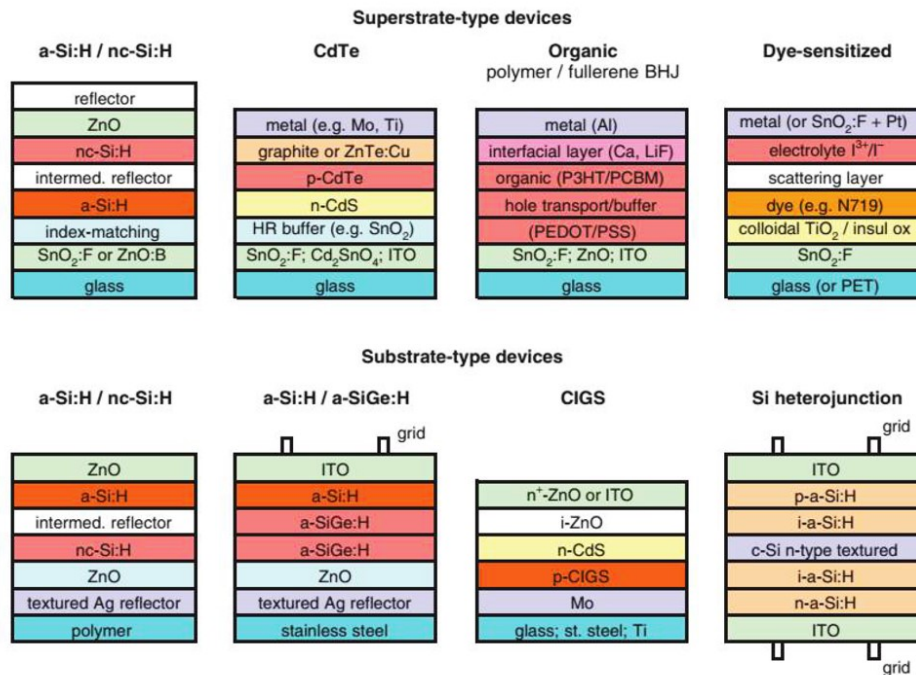


Figure 3. 5: Overview of photovoltaic devices using transparent conductive layers. Reproduced from (Delahoy & Guo, 2011)

The properties and physical parameters of each material and type of TCO depend on the deposition technique and the composition of such material. **Figure 3.6** shows a collection of different type of TCOs and their measured properties according to the technique of deposition (see (Dekkers, 2007) for detailed references). In such references, particular deposition techniques have been chosen in order to reach thickness uniformity, low production costs, and/or high yield. One big remark is related to the electrical and optical performance, which is not directly linked with the deposition technique, but to the intrinsic properties of the material as structure, morphology, and composition.

TCO	Deposition method	ρ (Ωcm)	T ^{II} %	FOM ($10^{-3}\Omega^{-1}$)	E _g (eV)	N	n (cm^{-3})	μ ($\text{cm}^2/\text{s/V}$)
SnO ₂	Spray	4.3×10^{-3}	97	1.45	4.11	2.2		
SnO ₂	Sputtering	6.1×10^{-3}	95	56.4	4.13		1.3×10^{20}	7.7
SnO ₂ :F	Spray	5×10^{-4}	>80		4.41		4.6×10^{20}	28
SnO ₂ :Mo	Reactive ev.	3×10^{-3}	>85	>0.07	4.10		8.0×10^{20}	10
SnO ₂ :Sb	Spray	10^{-3}	85	19.6	3.75		7.0×10^{20}	10
Cd ₂ SnO ₄	Sputtering	5×10^{-4}	>80			2.05	5.0×10^{20}	40
Cd ₂ SnO ₄	Sputtering	5×10^{-4}	93	34.6	2.7		5.0×10^{20}	22
CdIn ₂ O ₄	Sputtering	2.7×10^{-4}	90	69.7	3.24		4.0×10^{20}	57
In ₄ Sn ₃ O ₁₂	Sputtering	3.5×10^{-4}	>80		3.5	2.1	7.0×10^{20}	11.5
In ₂ O ₃	Thermal ev.	2×10^{-4}	>90		3.56		4.0×10^{20}	70
In ₂ O ₃	PLD	2×10^{-4}	86				9.0×10^{20}	37
In ₂ O ₃ :F	CVD	2.9×10^{-4}	>85	3.9	3.5			
GaInO ₃	Sputtering	2.5×10^{-3}	90	14			4×10^{20}	10
ITO	e-beam ev.	2.4×10^{-4}	90		3.85	2.0	8.0×10^{20}	30
ITO	CVD	1.7×10^{-4}	90	183	3.9		8.8×10^{20}	43
ITO	Sputtering	2.4×10^{-4}	95	70.4	4.0	2.0	1×10^{20}	12
ITO	PLD	8.5×10^{-5}	85	72.9			1.4×10^{21}	53.5
ITO	Sol-gel	5.0×10^{-3}					1.9×10^{20}	12
ITO:F	Sputtering	6.7×10^{-4}	>80	3.5			6.0×10^{20}	16
In ₂ O ₃ :Mo	Sputtering	5.9×10^{-4}	90	7.7	4.3		5.2×10^{20}	20.2
ZnO	Reactive ev.	10^{-3}	88		3.3		1×10^{20}	10
ZnO	Sputtering	2×10^{-3}	>80	4			1.2×10^{20}	16
ZnO:Al	Sputtering	10^{-2}	90		3.52		4.7×10^{20}	1.47
ZnO:Al	CVD	3.3×10^{-4}	85	49.2			8.0×10^{20}	35
ZnO:Al	PLD	3.7×10^{-4}	90	28.3	3.8	1.98	8.0×10^{20}	18
ZnO:Ga	Sputtering	10^{-3}	>85		3.59		10×10^{20}	10
ZnO:In	Sputtering	2×10^{-2}	>80	3.29		1.85	7×10^{19}	1.9
Zn ₃ In ₂ O ₆	PLD	1.0×10^{-3}	85		3.4		4.0×10^{20}	20
ZnSnO ₃	Sputtering	4×10^{-3}	>80				1×10^{20}	10

Figure 3. 6: Reported properties of n-type transparent conducting oxides. Re- produced from (Dekkers, 2007).

3.3 TCOs used in tandem cells

TCOs materials have been widely studied cause their transparency and electrical conductivity make them good candidates for front-side contact implementations. For instance, ITO or IZO (indium-doped zinc oxide) can be used in semi-transparent perovskite solar cells as it is reported in (Bett, et al., 2019), where TCOs can be directly sputtered on the hole conducting material, as it is shown in **Figure 3.7**. The goal of this work is to vary the parameters of sputtering of ITO over a structure, in order to improve the figures of merit, and the combination of this type of architecture provides an efficiency of around 24.2 %.



Figure 3. 7: Schematic structure of the perovskite solar cells using ITO. Reproduced from (Bett, et al., 2019)

Most advanced technologies have proved that ITO can be deposited using methods such as glancing angle deposition (GLAD), in which an inclined porous columnar nanostructure of ITO can be deposited and created. This kind of deposition allows the ITO to avoid the shadowing effect on a more atomic scale (see **Figure 3.8**). ITO introduction in tandem composed of amorphous silicon by this method has reported efficiencies ranging to 13.6 %, which can increase depending on the disposition of the bottom cell (Leem & Su, 2011).

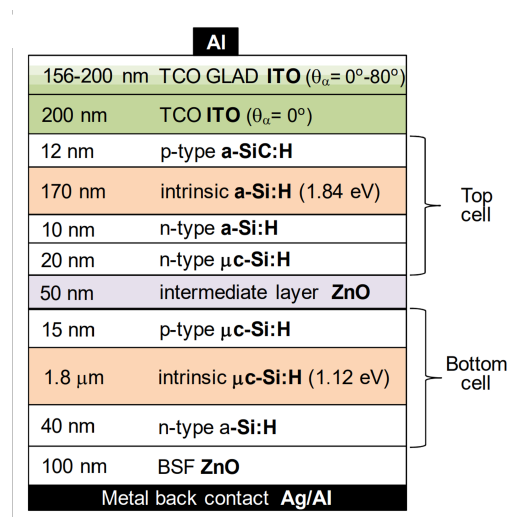


Figure 3. 8: Schematic diagram of the a-Si:H/ μ c-Si:H tandem tin film solar cells using ITO. Reproduced from (Leem & Su, 2011)

In the process of creating a transparent layer under the electrode, damages can occur, so it is possible to include a protective MoOx layer. As discussed ITO is one of the most TCOs used materials for top electrodes. A brief report of the advanced research over ITO on tandem cells includes the deposition of a 150nm thin layer of ITO to minimize the parasitic absorption in a 2T perovskite/Si tandem cell (Bush, et al., 2017), in which efficiency of around 23.6 % was reached (see **Figure 3.9 a.**). To reduce the reflection loss, a MgF_2 implementation on top of the cell as anti-reflection coating was designed, and in this way, efficiency of 25.7 was obtained by using an iBC c-Si bottom (Zhang, et al., 2018).

However, the optimization of efficiency is limited by the deposition process, since it is the main cause of damage to the next transporting layer. To solve this issue, a MoOx buffer layer in monolithic perovskite/Si solar cells was introduced (see **Figure 3.9 b.**) having a bi-layer front electrode of hydrogenated indium oxide and ITO that produces an optimized tandem cell in terms of carrier recombination reduction (Song, et al., 2016).

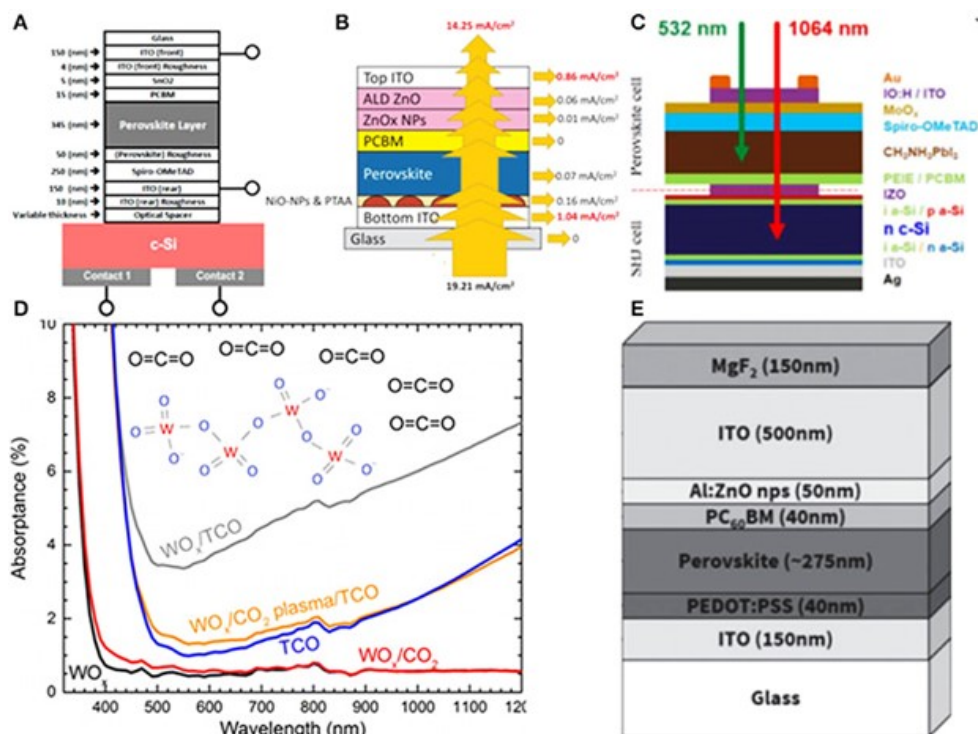


Figure 3. 9: Different configuration on solar cells architectures and D) absorption spectra of thick evaporated MoOx. Reproduced from (Leem & Su, 2011)

Other methods to reduce the sputtering damage and parasitic absorption of the ITO layer, can be related to a transition metal oxide working as a buffer layer as it is indicated in **Figure 3.9 E**). (Werner, et al., 2016)

It is important to remark that the evolution of the tandem cells can result in devices with a high EQE photocurrent and FF. Nevertheless, the parameters in the bottom cell using a combination of perovskite/Si are still far below the single junction c-Si with high performance. So, there is a window for improving such structures in order to maintain efficiency and at the same time, provide the trade-off between performance and production cost (Liu, et al., 2020).

CHAPTER 4: SIMULATIONS OF 4T TANDEM SOLAR CELL WITH ITO

The solar cell simulations presented for this thesis project are done using the software *Sentaurus*, a commercial software environment commonly used for the design and optimization of semiconductor devices. In this chapter is presented the implementation of TCO material in the software and its application in a 4T tandem cell as front/bottom contact.

4.1 Sentaurus TCAD

Sentaurus is a tool from *Synopsys* based on the Technology-Aided Design (TCAD). Sentaurus can perform simulations of fabrication, operation, and reliability of semiconductor devices. Sentaurus implements many detailed physical models to reproduce both the wafer fabrication and the single device operations, and it can be used to simulate a wide variety of semiconductor devices with the possibility of a deep analysis of the drawbacks and issues related.

The versatility and powerful environment in conjunction with a graphical user interface (GUI) to visualize the results, make Sentaurus one of the most used and performing software both by major companies and academic organizations, in areas such as: transistors (MOSFETs, TFETs, and FinFETs), power and memory devices, solar cells, and many others. Sentaurus offers a wide array of tools within the suite, each with a specific task in the simulation chain. Some of them will be presented in the following sections.

Sentaurus workbench (SWB)

The workbench of Sentaurus is the graphical front end that integrates all the TCAD Sentaurus simulation tools into one environment. The main activities of this tool are: to design, organize and run simulations, with the possibility to perform sweeping on many parameters. Furthermore, SWB can link and access all the tools and variables that compose the projects.

Figure 4.1 shows the graphical interface of the software.

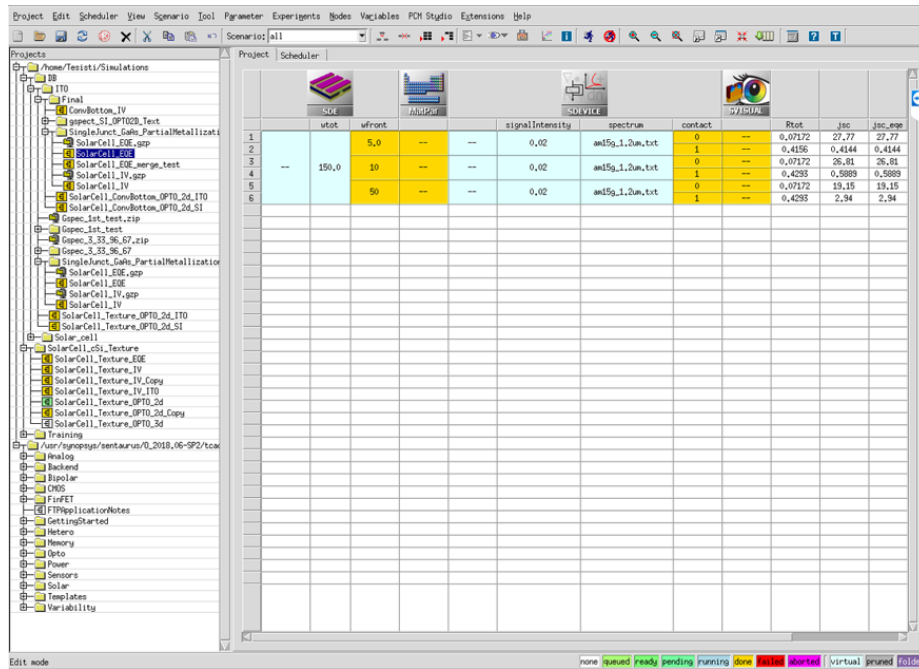


Figure 4. 1: Sentaurus TCAD workbench graphical environment.

Sentaurus device editor (SDE)

The structure device editor of Synopsys comprehends the creation and editing of 2D/3D structures by simple blocks. This tool also helps the user to provide a more complex definition of the materials, giving them a complete geometry, doping, meshing, and refinements, among others. The interface as well as the scheme commands can be observed in **Figure 4.2**. The tools also include the creation of the simulation mesh, which is a crucial point in the process since all the calculations depend on the meshing grid. The structure must be well- defined in order to be received by the *sdevice* tool so that the geometry will not influence future errors for the calculations and also the meshing process will affect the trade-off between the computational time and the accuracy of the simulated results.

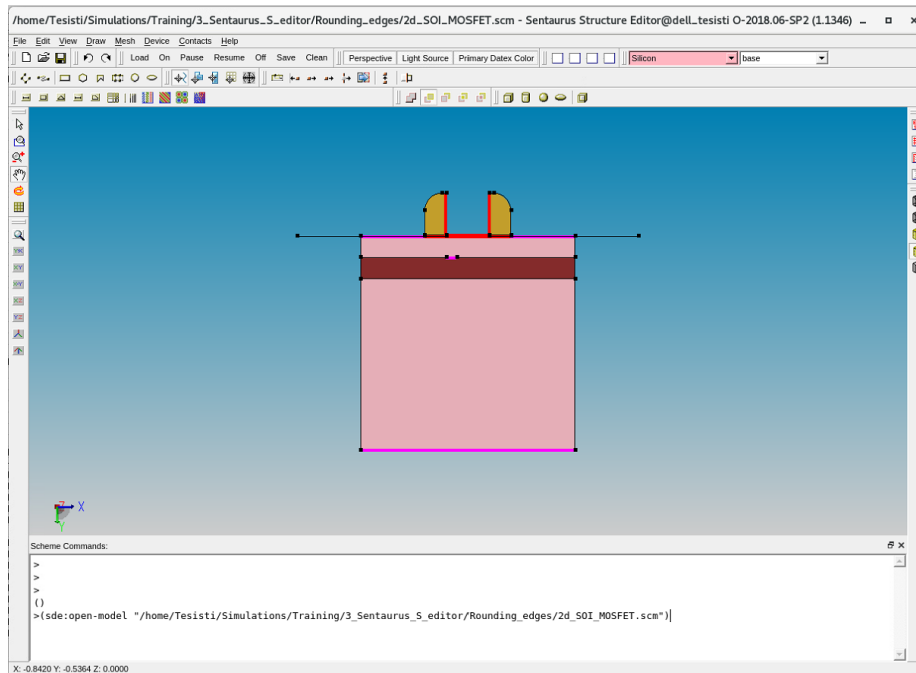


Figure 4. 2: Sentaurus Device Editor with a simple 2D MOSFET.

Sentaurus device (SDEVICE)

Sentaurus Device is a semiconductor device simulator compatible with 1D/2D and 3D geometries. Sdevice can simulate the electrical, thermal, and optical characteristics of most semiconductors (silicon, germanium, and silicon carbide are the most used ones), compound semiconductor devices, organic materials, and chalcogenide alloy devices. The versatility to work with compounds such as GaAs, InP, AlGaAs, and so on, confirms the good compatibility with solar cells. Sdevice is the tool that actually performs electrical and optical simulations, implementing and activating different models based on the most important physical phenomena involved in the simulated device. It is also possible to change and sweep parameters and variables, allowing to carry out a complex analysis in this phase. Observe (**Figure 4.3**) that in this section the variable section is very important, since it can work with different input files, constant parametrization, and models.

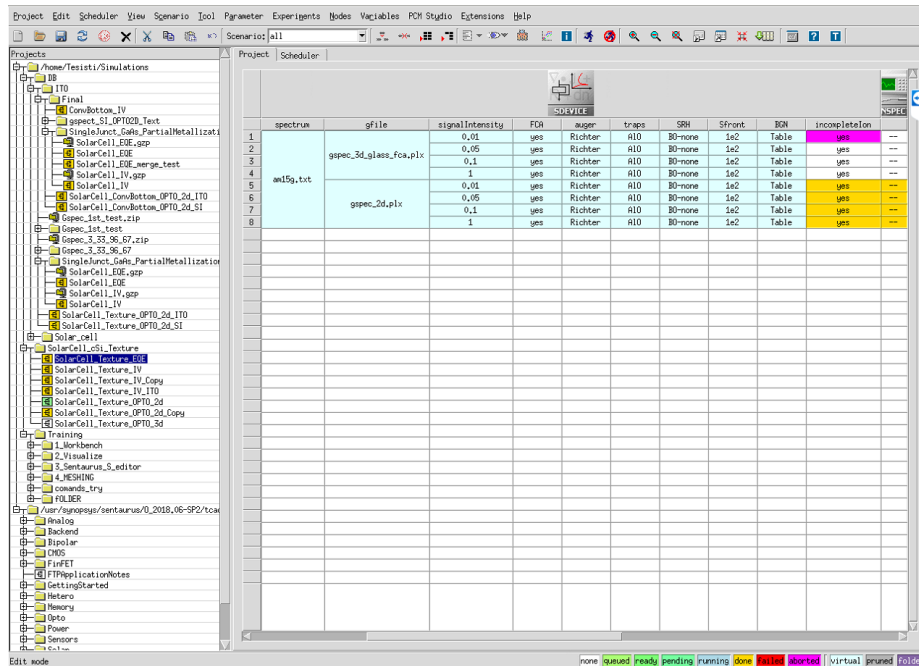


Figure 4. 3: Sentaurus Device in a complete analysis of a solar cell.

4.2 Introduction of ITO in Sentaurus

Sentaurus already offers a wide variety of materials very well characterized and studied, however, the transparent conductive oxides are not present in the list included with the software. To introduce a new material in the database of Sentaurus, it's important to collect most of the physical parameters that will be used in simulations, define its electrical behavior and correctly introduce it within the database.

Normally, in the command window of each single tool (sde and sdevice) the needed parameters must be defined, and that's the simple way to include a material. In the case of a new material, it has to be defined as an insulator, conductor, or semiconductor as it is shown on the left of **Figure 4.4**, where the color is given in hexadecimal format. Once it is added into the database of Sentaurus, the software must recognize it and appear on the list of materials, as shown in the created rectangle of **Figure 4.4**.

At this point, the material is recognized to create any desired structure, providing a suitable parameter file that can be used by the sdevice simulator tool. To calibrate the ITO

behavior an ITO/C-Si structure (see **Figure 4.5**) was taken as reference, in which ITO growth parameter is experimentally varied to characterize its property changes. All the parameters for crystalline silicon were already included in Sentaurus, and it can be reviewed in (Green & Keevers, 1995).

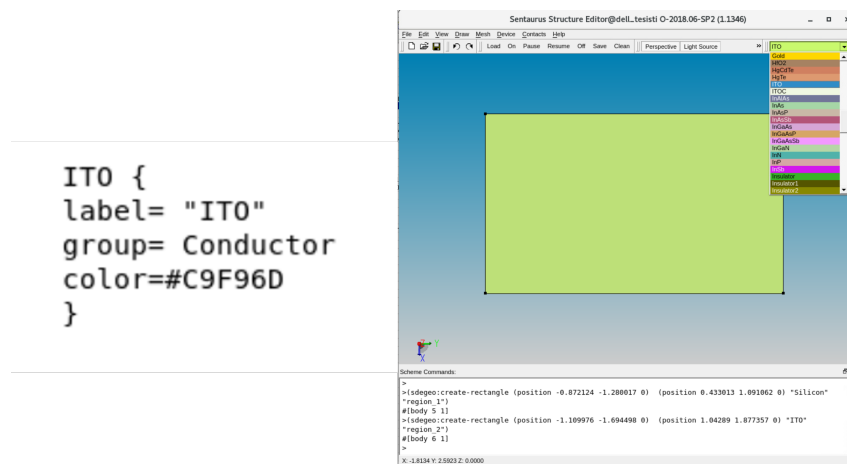


Figure 4. 4: Implementation of ITO in Sentaurus device editor.

To repeat such structure, a layer of ITO was parameterized from 0 to 50 μm , as it is shown in **Figure 4.6**, where is it possible to appreciate the parameter section called *ITOT* relative to the thickness of the ITO layer, and the structure performed on Sentaurus device structure. Both terminals are made of Aluminum and Silicon as the bottom layer section.

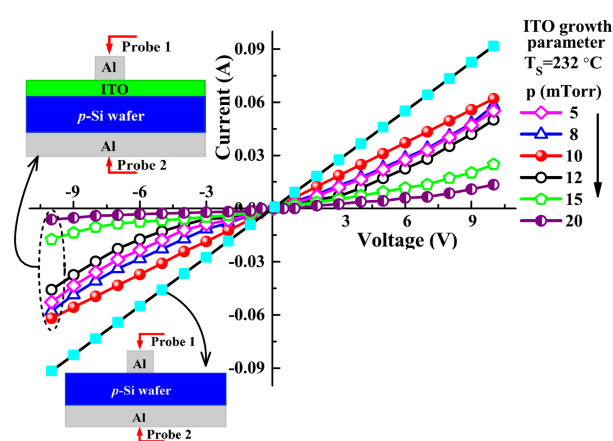


Figure 4. 5: Current-voltage characteristics of p-type c-Si wafer/ITO junctions (Das & Karmakar, 2019)

The sdevice section will perform the voltage-current (IV) curve by introducing the parameters of ITO. In order to do this, the sdevice tool has two ways to implement the material, and both are shown in **Figure 4.7**. The first one is to right-click in the sdevice square and select

Edit input → *Parameters or Include Materials*, after that is very important to indicate the root of the *ITO.par*, which is the parameter file that contains all the physical parameters of ITO, normally this file must be placed in the same folder as the current project. The second way is to introduce ITO in sdevice, consisting of entering in the *Include Materials* section, where a window will display all the materials incorporated in the software, it is enough to click on *ITO*.

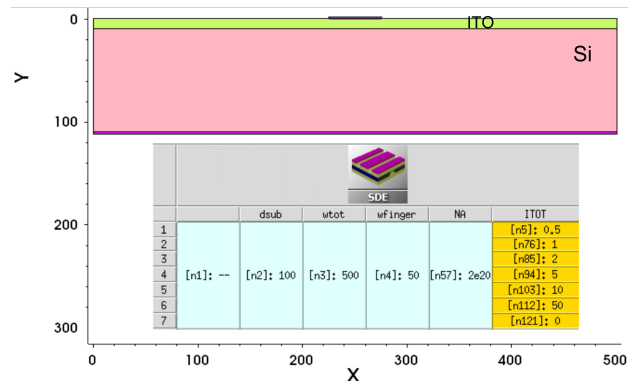


Figure 4. 6: ITO/c-Si single junction performed in Sentaurus.

The variation in the ITO thickness can be associated with the difference in the ITO growth parameter by varying it from zero, in which it will behave as a non-ITO layer. In this case the current must be larger since there is no material at the top of the silicon which can present resistive effects, and this can be observed in the IV results given in **Figure 4.8**. As the thickness of ITO grows, the layer will show more resistance to the flow of electrons, decreasing the current, the larger the ITO layer traps the less current through the junction, this is compared also in the same plot, which is produced in another tool of Sentaurus called *Inspect*.

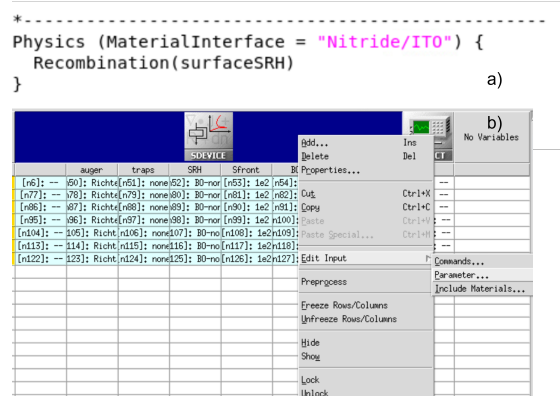


Figure 4. 7: Sdevice section to introduce ITO material.

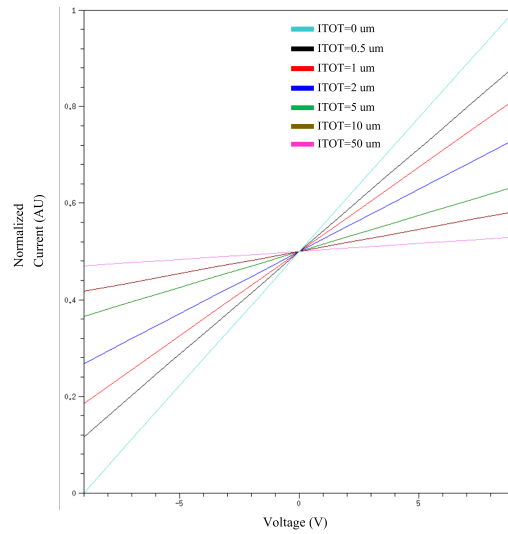


Figure 4. 8: Current-voltage curve obtained for the structure given in **Figure 4.7**

4.3 4T Tandem cell simulation

The goal of the TCAD simulations performed in this work was to test the ITO implementation in a 4T tandem cell. A study of the performance of ITO contact instead of aluminum one in different conditions was conducted. They were also evaluated ITO's best trade-off in relation to changes in thickness or width of the top and bottom contacts. The simulated 4T tandem cell is shown in **Figure 4.9**.

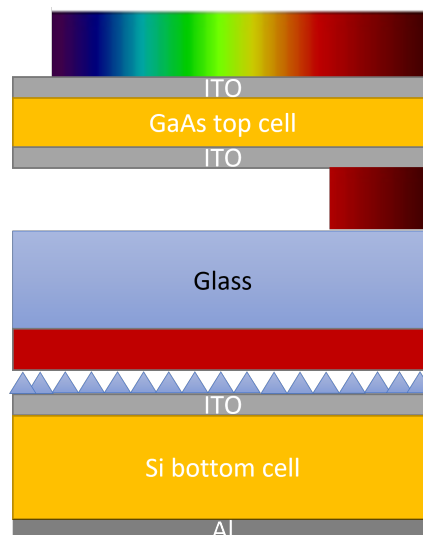


Figure 4. 9: Schematic of the simulated 4T tandem solar cell in TCAD Sentaurus.

Given the characteristics of the architecture used, the electrical simulations for the top and bottom cells were performed separately. The upper cell used was a GaAs III-V thin film solar cell, while the lower was a conventional c-Si cell. The optical output of the top cell was used as input for the bottom cell, to simulate the coupled optical behavior. The contacts of the top cell and the front contact of the bottom one, usually made of aluminum, were replaced by ITO.

4.4 GaAs cell simulation

The top cell of the 4T tandem cell is a thin-film structure of gallium arsenide. One of the characteristics of this type of cell is its high bandgap, better suitable for the absorption of the more energetic photons, while almost transparent to the higher wavelength that would be absorbed in the bottom section of the tandem cell. To understand this behavior, two simulations were carried out, the first one is the electrical analysis, in which the I-V and P-V characteristics curves were analyzed by tuning the width and thickness of the contact. The second one is related to the optical analysis, which provided the spectral reflectance and its counterpart, the transmittance. The structures of the top cell varying the top width is shown in **Figure 4.10**, in the same way, the structures of bottom cell varying its width is given in **Figure 4.11**.

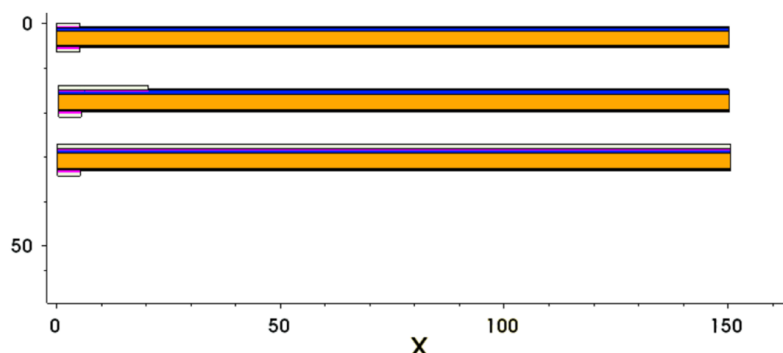


Figure 4. 10: Variation on front contact ITO width (5-20-150 μm) in top cell.

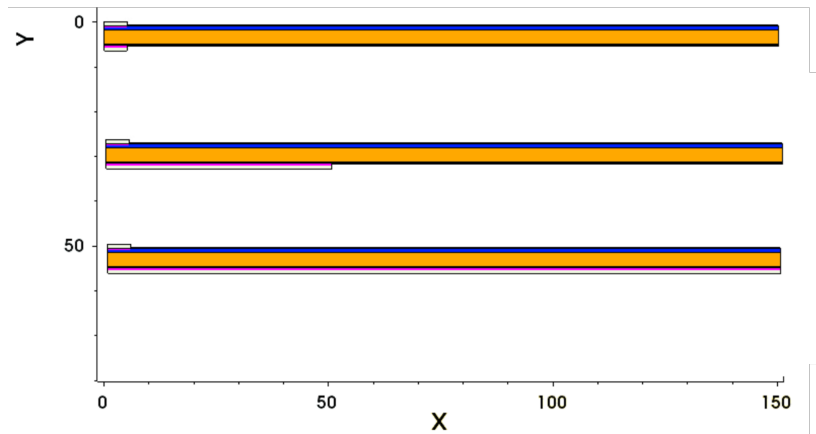


Figure 4. 11: Variation on bottom contact ITO width (5-50-150 μm) in top cell.

4.4.1 Electric/Optic GaAs cell simulation

Using the visual tool of Sentaurus, it was possible to extract the electric and optic characteristics of a solar cell, either with aluminum or ITO as front contacts. Regarding the electric simulation, the I-V and P-V characteristics were produced under illumination, as a function of applied voltage. The IV curve of a top GaAs solar cell with some aluminum as top contact is given in **Figure 4.12**.

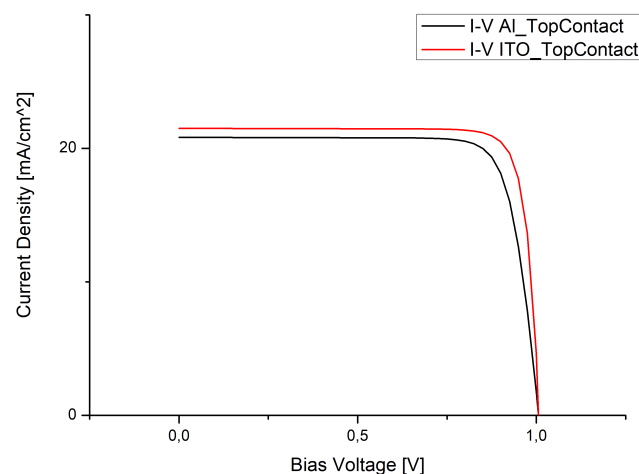


Figure 4. 12 I-V curves for a top GaAs solar cell using Aluminum and ITO as top contact :

In order to achieve a good I-V curve and compare it with the aluminum contact, in **Figure 4.12**, for a cell using ITO as front contact, a well-optimized thickness and width is

provided in **Figure 4.12**, in which a front contact width was set to be $20 \mu\text{m}$, the bottom contact width is $150 \mu\text{m}$, and both top and bottom contact thickness are $100 \mu\text{m}$.

The figures of merit obtained for both compared configurations are photo-generated current density (J_{ph}), short-circuit current density (J_{sc}), open-circuit voltage (V_{oc}), power density (P_{mpp}), current density (J_{mpp}), and voltage (V_{mpp}) at the point of maximum power, Fill Factor (FF) and efficiency (η). The values of such figure of merit are shown in **Table 4.1**. It is possible to observe a slight improvement in the cell using ITO, since the ITO configuration was the most optimal one given by the different ratios of width and thickness simulated.

Cell	J_{sc}	V_{oc}	P_{mpp}	V_{mpp}	J_{ph}	Fill Factor	Efficiency
Al	27.76	1.006	0.85	22.66	28.59	81.13	22.66
ITO	28.66	1.006	0.9	24.6	29.61	85.34	24.6

Table 4. 1: Figures of merit for Al and ITO top cell configuration.

Optical simulation of GaAs top cell

The optical analysis of the cell was performed using the "bias light" method, in which the cell is illuminated with the AM1.5g solar spectrum. Using again the tools of sdevice and svisual, it was possible to obtain the different characteristic of an optical simulation, which are reflection, transmission, and absorption of the cell.

The transmittance of both cells (see **Figure 4.13**) shows of aluminum and ITO is lower in almost all the spectrum until 800 nm. After this wavelength, there is a high transmittance in the spectrum, which makes both materials good for tandem applications. The main difference that can be seen is a smoother transmittance curve in the case of aluminum, given by the fact that in that case only a fraction of the bottom surface was covered by the metal, to allow the lightest to pass in the bottom cell without degrading the bottom contact resistance too much. In the case of optimal ITO configuration instead, given the almost transparency of the material, it was used a complete cover of the bottom surface, in order to achieve better electrical

performance in terms of resistance but without losing the possibility to absorb the remaining portion of light in the bottom cell.

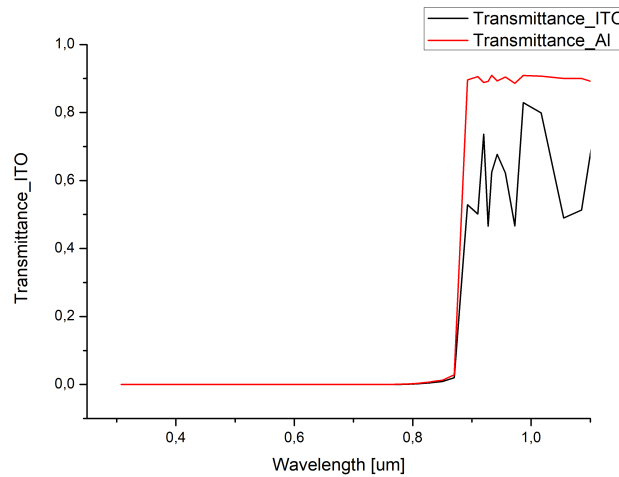


Figure 4. 13: Transmittance spectra of aluminum and ITO-based solar cells.

The transmittance spectrum simulated in the top cell was then multiplied for the overall AM1.5G spectrum, in order to obtain the actual light spectrum that passed through the top cell and reached the bottom one, as shown in **Figure 4.14**.

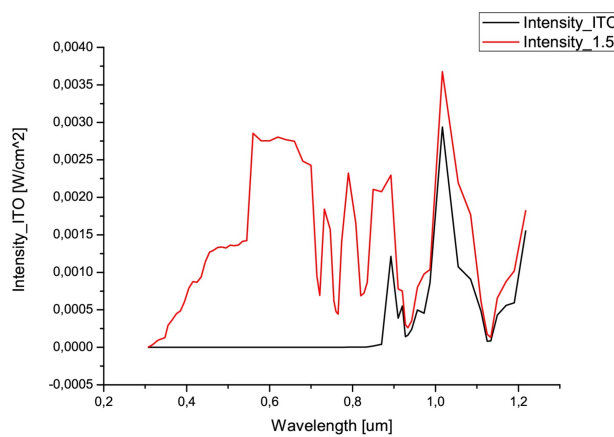


Figure 4. 14: AM1.5g spectrum and GaAs cell output spectrum using ITO as top contact.

4.5 Silicon bottom cell simulation

The simulated bottom cell was a single-junction crystalline silicon type, electrically separated from the top GaAs cell. It is important to remark that, the structure overall is still a tandem cell, which means that the lower cell will absorb the remaining photons that are not absorbed by the upper cell.

The output spectrum of the top cell was used to create an optical generation profile over a simple structure that contains a symmetry element (that can be reproduced exactly over the whole cell) of a silicon cell with pyramidal texturing (this last texturing was done in order to reduce the surface reflectance of a plane structure). After that, the obtained optical generation profile was used as input for the electrical simulation of the symmetry element of the complete Si cell.

In order to obtain the optical generation profile, it was considered a structure including glass and ethylene vinyl acetate layers on the textured bottom cell, to take into account the actual structure of a tandem cell. **Figure 4.15** shows the two-dimensional symmetry element used for simulating the crystalline silicon cell.

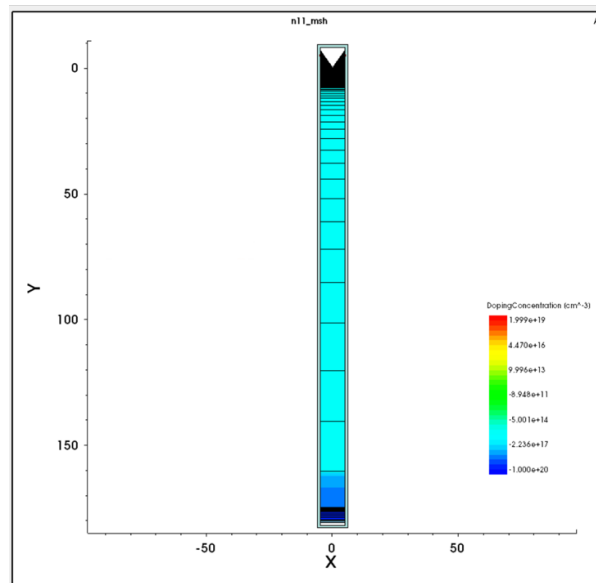


Figure 4. 15: 2D symmetry element of c-si solar cell

To perform the optical analysis in the device section, a Monte Carlo ray-tracing method was used, in which the transmission and reflection coefficients (T and R) of the ray at the interface are calculated. Then, a random number r is generated such that if $r < R$, only the reflected ray is propagated, otherwise only the transmitted ray is propagated. It is also possible to define the initial number of beams and also the limit one, in which the analysis will stop.

- **nrays**: initial number of beams (set to be 10000)
- **depthlimit**: sets the maximum depth interface that ray can cross.
- **minintens**: sets the lowest intensity value that a ray can have, before being considered lost.

The wavelength was varied to cover the whole spectrum so that raytracing can be done in each single wavelength value. One reflectivity value of the side walls was fixed, in a way such that all rays remained confined inside the symmetry element considered. This approximation neglects edge effects but is acceptable. In this structure, two optical generation files were needed, since the ITO section, working as front contact of the bottom cell, has different optical properties than the rest of the cell not covered with ITO, so from the two generation profiles was created a weighted average according to the proportion of the specific simulation (5:150, for example, being one the ratio of ITO contact over the whole pitch).

The different models used in the simulation are the following: For the bandgap model, it was used the "Slotboom" model (Slotboom & De Graaf, 1976), which depends on the temperature of the crystal such that:

$$E_g(T) = E_{g,0} + \delta E_{g,0} - \frac{\alpha T^2}{T + \beta} \quad (4.1)$$

The effective bandgap is obtained using the previously obtained bandgap.

$$E_{g,\text{eff}} = E_g(T) - E_{bgn} \quad (4.2)$$

Where E_{bgn} is the narrowing bandgap. It is also used the electronic affinity:

$$\chi(T) = \chi_0 + \frac{(\alpha + \alpha_2)T^2}{2(T + \beta + \beta_2)} + B_{gn} 2 \text{ Chi} \cdot E_{bgn} \quad (4.3)$$

The bandgap narrowing inside the Sentaurus Device is written as:

$$E_{bgn} = \Delta E_g^0 + \Delta E_g^{\text{Fermi}} \quad (4.4)$$

In which, E_g^{Fermi} is the corrective factor that introduces the carrier statistics. And, the ΔE_g^0 is equal to:

$$\Delta E_g^0 = E_{ref} \left[\ln \left(\frac{N_{Tot}}{N_{ref}} \right) + \sqrt{\left(\ln \left(\frac{N_{Tot}}{N_{ref}} \right) \right)^2 + 0.5} \right] \quad (4.5)$$

For silicon values, the following parameters were used (See **Figure 4.16**):

Parameter	Value	Unit
$E_{g,0}$	1.1696	eV
$\delta E_{g,0}$	-4.795×10^{-3}	eV
α	4.73×10^{-4}	eV/K
α_2	0	eV/K
β	636	K
β_2	0	K
χ_0	4.05	eV
<i>Bgn2Chi</i>	0.5	1
E_{ref}	6.92×10^{-3}	eV
N_{ref}	1.3×10^{27}	cm^{-3}

Figure 4. 16: Silicon parameters for the optic simulation of bottom cell

The complex refractive index related model was also used, which employs wavelength-dependent refractive indexes and extinction coefficients. In simulations using the ITO complex refractive index, the values were taken from (Polyanskiy, 2022).

The Inspect tool of Sentaurus was used to create the output spectral generation profile.

- N_{illu} : number of incident photons on the cell.
- N_{top} : number of the reflected photons over the surface of the cell.
- N_{bottom} : number of transmitted photons.
- N_{abs} : number of absorbed photons.

The reflection, transmission, and absorption over the whole region were calculated using the following relations:

$$R(\lambda) = \frac{N_{top}}{N_{illu}} \quad (4.6)$$

$$T(\lambda) = \frac{N_{bot}}{N_{ilu}} \quad (4.7)$$

$$R(\lambda) = \frac{N_{abs}}{N_{ilu}} \quad (4.8)$$

4.5.1 IV bottom cell simulation

The bottom cell simulated consists of an n-type emitter and p-type base, with a layer of ITO at the top and full contact of aluminum at the bottom, as it is shown in **Figure 4.17**. Some of the parameters needed to make the structure were set in the Workbench, namely the height of the cell, the width of the finger, the doping level of the base, emitter, and back surface field (BSF, that is a higher doped region at the rear surface of the solar cell), and the depth of the emitter and BSF.

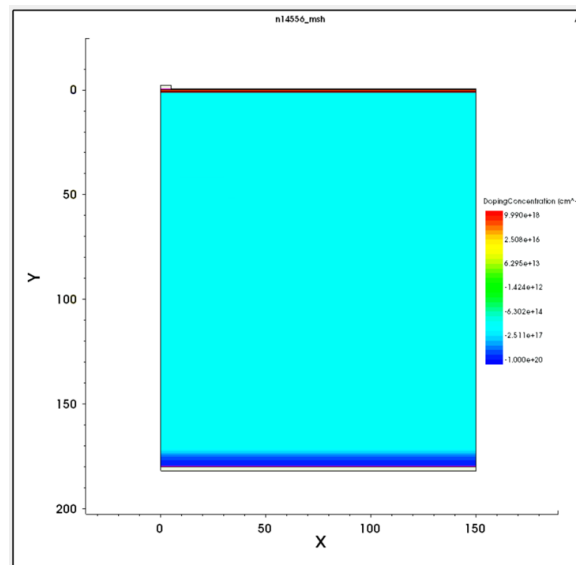


Figure 4. 17: Structure of the silicon bottom cell

To obtain the I-V characteristic in this cell, the anode voltage was made to increase in two "quasistationary" statements, in order to increase the resolution around the point at maximum power and the steeper portion of the curve. Larger steps were done until 0.45V, and shorter ones, and thereby more precise, until 0.9V. Once again, the figure of merit were obtained using the inspect tool. Both bottom configurations (with ITO and Al as front contact)

IV characteristics are plotted in **Figure 4.18**. Notice that even in this case the best configuration for ITO was slightly better than the aluminum one.

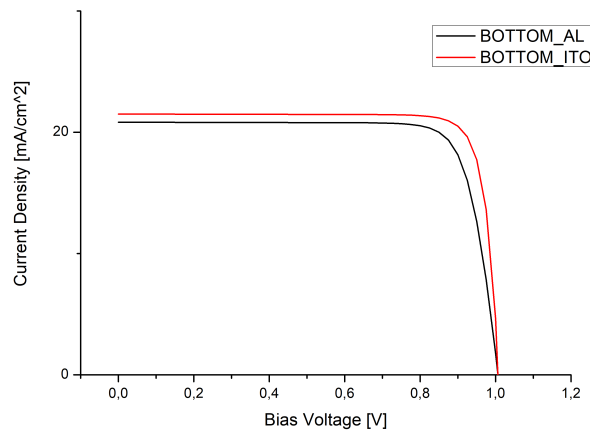


Figure 4. 18: I-V characteristic for the bottom cell configuration using ITO and Al as contacts

4.6 Results on tuning parameters

In order to evaluate the results provided by the different configurations, the figures of merit of a solar cell are studied. The starting point on the top cell is the figure of merit for the GaAs cell using aluminum and ITO as top/bottom contacts respectively. **Table 4.2** shows the four results to be evaluated as a function on variation of geometry of top and bottom ITO contact. Basically, the idea under this variation is to sweep the four different geometrical factors of the ITO contact. Those values, either thickness or width are: ITO front contact top cell, ITO rear contact top cell, ITO front contact bottom cell, and ITO rear contact bottom cell.

Cell	Jsc	Voc	Fill Factor	Efficiency
Al	27.76	1.006	81.13	22.66
ITO	28.66	1.006	85.34	24.6

Table 4. 2: Figures of merit for Al and ITO top cell configuration

The width and thickness of top and bottom contacts are interesting parameters that impact directly on the figure of merit. In order for a layer of ITO to be used as contact, it has to present a good trade-off between the optical and electrical properties. In this scenario, it is

possible to simulate the figures of merit of the top cell with a sweep on the following parameters: top contact width, top contact thickness, bottom contact width and bottom contact thickness. The values used are displayed in **Table 4.3**.

Sweep	Range [μm]
Top Contact Width	5,20,50,75,100,150
Bottom Contact Width	5,10,50,75,100,150
Top Contact Thickness	10,50,100
Bottom Contact Thickness	10,50,100

Table 4. 3: Values used to sweep the variables on the ITO contacts.

Variation on ITO front contact width of the top cell

The first sweep was carried out by varying the top contact width, and **Figure 4.19** shows the figures of merit of every single configuration. The comparison point will always be the aluminum figure of merit obtained previously in **Table 4.2**. In the current result, it is possible to observe that the top contact presents good results when not fully covered (less than $50 \mu\text{m}$), and the variations in terms of efficiency show that after a top width larger than approximately $50 \mu\text{m}$, the ITO top contact is not better than aluminum and any other configuration. This can mainly be ascribed to the trade-off between the ITO optical absorbance, which reduces the amount of light collected, and the resistance behavior that improves with larger areas of contact. Notice that the change in efficiency comparing the $20 \mu\text{m}$ with $50 \mu\text{m}$ is relatively low, so it is up to consider choosing the optimal width of the top contact. Area, economical factors, and mechanical consistency must be taken into account in order to deposit a layer of ITO at the surface of the solar cell.

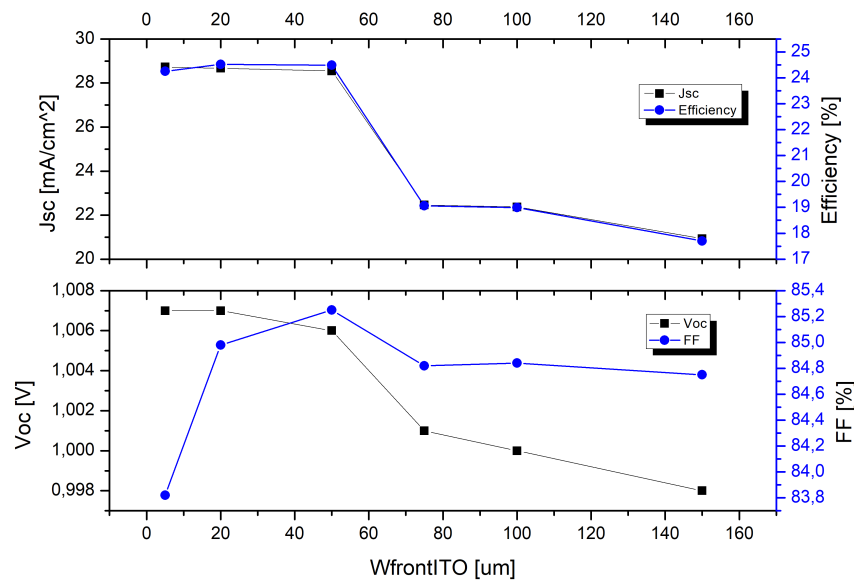


Figure 4. 19: Figures of merit variations due the sweep of the front contact width.

Variation on ITO bottom contact width of the top cell

The second sweep is related to the variation of the bottom contact width, **Figure 4.20** shows the figures of merit of every single configuration. Again, the variation is done in order to compare with aluminum contact performances. In this case, is appreciable that the best configuration is the one with a completely covered bottom surface. This is due to the fact that the maximum efficiency of the top cell was considered the best possible outcome, without at the same time taking into account the reduction of the light that will go through on the bottom cell. This is validated by the fact that most of the collected light and therefore the efficiency of a 4T solar cell comes from the upper cell, so it is reasonable to aim for the best performance there. An interesting evolution of this work could include a complementary evaluation of the electrical and optical properties of both cells combined, to understand if this is true in any configuration. In this scenario, and considering the top contact set to $20 \mu m$, the best architecture possible is the one fully covered with ITO at the bottom. It is also worth noticing that for bottom contact widths between $1-10 \mu m$ there is a lower performance than using conventional aluminum contact, and so in the case of limiting factors in the fabrication, it is not recommended the use of ITO.

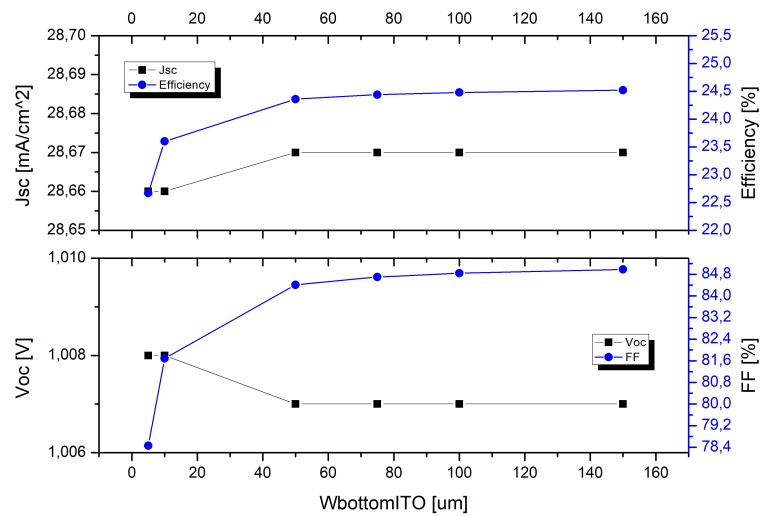


Figure 4. 20: Figures of merit variations due the sweep of the bottom contact width

Variations on ITO front/bottom contact thickness of the top cell

The third and fourth sweeps consisted of varying the thickness of the ITO either and top or bottom contacts. Those architectures show that all configurations larger than 10 μm will provide a better figure of merit than aluminum. The interesting fact lies in how much changes the efficiency after doubling the amount of material at the top and bottom contacts. Notice that after 10 μm of thickness, the efficiency is almost constant. Thereby, in terms of efficiency, will be better to have the thickest layer, however, it will not give a good trade-off since the ITO layer must remain as thin as possible to reduce light absorption. The recommendable values, in this case, are the configurations within 10 μm and 50 μm .

Contact thickness [μm]	ITO Top efficiency	ITO Bottom efficiency
10	24,13	24,13
50	24,52	24,15
100	24,57	24,15

Table 4. 4: Values used to sweep the thickness of the ITO contacts.

ITO front contact of bottom cell variations

The last parameter variation was related to either the width or the thickness of the ITO top contact that belongs to the bottom crystal silicon cell. It is very important to notice that the

spectrum that arrives at the surface of the bottom cell is greatly limited by the top cell absorption and so the figure of merit will be reduced with respect to a stand-alone cell. Hence even the optimal values and the optimization process can change. In this framework, the sweep of the top contact width is the most important, since it provides information that can be compared with the top cell optimization. **Figure 4.21** shows the FOM trends changing the top contact width in the bottom cell in tandem configuration. The sweep was performed using a thickness of $100\mu\text{m}$ since the advantages of this value were previously shown.

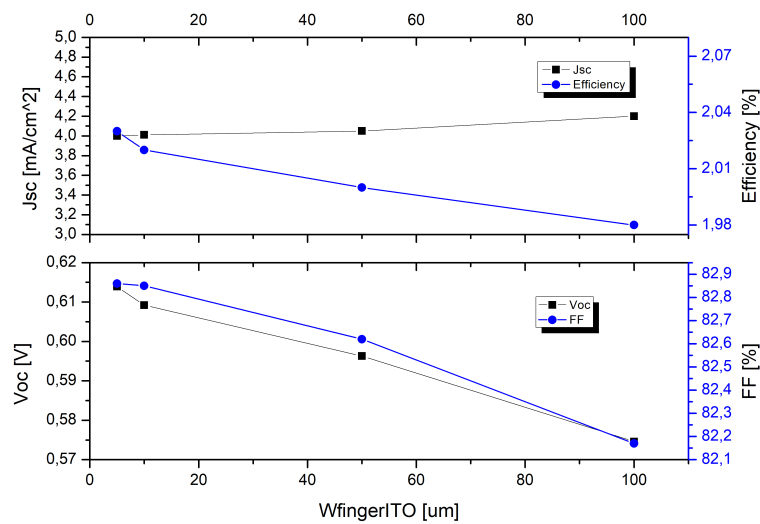


Figure 4. 21: Figures of merit variations due to the variation of the top contact width of bottom cell width.

It is possible to observe in the results that the figures of merit decrease as the ITO width increases, but in general, they are mostly constant except for minor variations, the most notable being the decrease of Voc probably due to higher recombination at the front surface. In this case, with a much-reduced illumination spectrum, it's possible to notice a negligible effect of the higher absorbance on the Jsc and also the slight decrease of the fill factor due to the higher linear resistance effect. In this configuration, the best performance, which is still higher than using an aluminum contact (efficiency=1.95%), comes from using a small width contact, in the order of a few μm .

4.7 Overall figures of merit for a 4T tandem solar cell with ITO contacts

The carried out simulations of a 4T cell showed that the use of a tandem cell allows a substantial improvement in the conversion energy since the two different cells can work together, exploiting more efficiently a larger part of the illumination spectrum. Additionally, it was studied the effect of introducing a transparent oxide as contacts instead of the conventional metal ones. Variations over the geometrical parameters of the indium tin oxide contact were performed, in order to optimize them for the best possible performance.

The optimized figures of merit of the 4T tandem cell simulated in this work are given in **Table 4.5**. Those values are the most optimal in terms of the width and thickness of the different ITO configurations. As discussed earlier, the trade-off between these two geometrical parameters must be carefully considered in the design of a solar cell, even more so considering the possibility to change the TCO properties in the fabrication phase. The final considerations found from the simulations are that the top contact should not cover the entire front surface in both cells, showing a trade-off between absorption and electrical conductivity. Finally, it is important to remark that the efficiency of the bottom cell can be optimized by tuning the intrinsic parameters of ITO, so the total configuration performance could be increased further.

Cell	$J_{sc} \left[\frac{mA}{cm^2} \right]$	$V_{oc} [mV]$	FF[%]	Efficiency [%]
GaAs/ITO Top Cell	28,66	1,006	85,34	24,6
ITO/Si Bottom Cell	4,00	0,614	82,86	2,03
ITO/GaAs/Si tandem cell				26,63

Table 4. 5: Final figure of merit of a 4T tandem solar cell using ITO as contacts.

CONCLUSIONS

Transparent conductive oxides (TCOs) are getting more and more attention in the development of photovoltaic devices, particularly in the design of complex architectures, given their intrinsically advantageous electrical and optical properties. In recent years the study and optimization of this class of materials have gained paramount importance in the process of improving the performance and reducing the costs of solar cell fabrication.

This work of thesis employs a double approach to the applications of TCO in a photovoltaic context. The state-of-the-art about this category of materials has been presented and also, as an experimental project, simulations of a four-terminal tandem solar cell implementing Indium-Tin-Oxide (ITO), the most used TCO material, have been conducted.

The 4T tandem cell was described in terms of its working principle, characteristics, and figures of merit. The configuration of the simulated tandem cell consisted of a top cell made of ITO/GaAs and a bottom cell constituted by ITO/c-Si. The optical and electrical simulations of the tandem cell were performed independently but optically coupled, which means that, in order to simulate the bottom cell, the transmission spectrum of the top cell was used as an input for the ITO/c-Si cell. After this, a comparison with the same structures using aluminum was performed in order to evaluate the figures of merit of a single cell.

Different variations in terms of width and thickness of ITO contacts were simulated to obtain the best configuration, and the results indicated that the cell with the highest efficiency of around 26,63 % was obtained with a front contact width (in the top cell) in a range of 20-50 μm , and thickness of about 50 μm and bottom contact fully covered. Furthermore, it was shown that, with the goal of maximizing the efficiency of the top cell, particular consideration must

be taken in designing a less covered front surface but maintaining a good trade-off with the contact resistance.

In general, it has been shown that the use of TCO materials, especially in 4T tandem solar cells, has already and will surely continue to bring benefits and improvements in the overall performance of PV systems. With the advancements in the research, future works may delve deeper into this optimization process by considering an interdependent approach in the design of the light management between the two cells composing the tandem architecture, in particular considering the transparency advantages of the TCO with respect to the conventional metallic contacts.

REFERENCES

- NASA. (2012). *NASA/Goddard*. Retrieved from The Sun Layers: https://www.nasa.gov/mission_pages/sunearth/multimedia/Sunlayers.html#
- Smets, A., Jägger, K., Isabella, O., Swaaij, R., & Zeman, M. (2015). *Solar Energy: The physics and engineering of photovoltaic conversion, technologies and systems*. UIT Cambridge.
- Callozzo, A. (2011). *"Numerical simulation of interdigitated back contact hetero-junction solar cells"*. Doctoral Dissertation.
- Smerlak, M. (2011). A blackbody is not a blackbox. *European journal of physics*(32.5), 1143.
- International, A. (2021). Retrieved from Standard Tables for Reference Solar Spectral Irradiances: <http://www.astm.org/DATABASE.CART/HISTORICAL/G173-%2003.htm>.
- Simon, M., Yiming, L., & Kwok, K. (2021). *Physics of semiconductor devices*. John wiley & sons.
- Michalopoulos, P. (2002). *A novel approach for the development and optimization of state-of-the-art photovoltaic devices using Silvaco*. Monterey: Naval Postgraduate School.
- Kalogirou, S. A. (2013). *Solar energy engineering: processes and systems*. Academic press.
- Base, E. D. (2021). *Periodic Table of Elements* . Retrieved from Element Database: <http://www.elementsdatabase.com>
- Basnet, P. (2015). *Metal oxide photocatalytic nanostructures fabricated by dynamic shadowing growth*. University of Georgia: Doctoral Dissertation.
- Learning, L. (2022). *History of QUantum Mechanical Quantities*. Retrieved from Lumen Learning: <https://courses.lumenlearning.com/boundless-ph%20ysics/chapter/history-and-quantum-mechanical-quantities/>
- Würfel, P., & Würfel, U. (2016). *Physics of solar cells: from basic principles to advanced concepts*. John Wiley & Sons.
- Schlangenotto, H., Maeder, H., & Gerlach, W. (1974). Temperature dependence of the radiative recombination coefficient in silicon. *Physica status solidi* , (a)(21.1), 357-367.
- Maccaronio, V. (2017). *Design of interdigitated back-contact solar cells by means of TCAD numerical simulations*. Doctoral dissertation.
- Shockley, W., & Read, W. (1952). Statistics of the recombinations of holes and electrons. *Physical review*, 87.5, 835.

- Hall, R. N. (1952). Electron-hole recombination in germanium. *Physical review*, 387.
- Green, M. A. (1982). Solar cells: operating principles, technology, and system applications. *Englewood Cliffs*.
- Shockley, W. (1949). The Theory of p-n Junctions in Semiconductors and p-n Junction Transistors. *Bell System Technical Journal*, 435-489.
- Ravindra, N., & Prasad, B. (1980). Saturation current in solar cells: an analysis. *Solar Cells*, 109-113.
- McEvoy, A., & Markvart, T. (2003). *Practical handbook of photovoltaics: fundamentals and applications*. Elsevier.
- Bartesaghi, D., Pérez, I. D., Kniepert, J., Roland, S., Turbiez, M., Neher, D., & Koster, L. (2015). *Competition between recombination and extraction of free charges determines the fill factor of organic solar cells*. *Nature communications*.
- Shockley, W., & Queisser, H. J. (1961). Detailed balance limit of efficiency of p-n junction solar cells. *Journal of applied physics*, 510-519.
- Chapin, D. M., Fuller, C. S., & Pearson, G. L. (1954). A new silicon p-n junction photocell for converting solar radiation into electrical power. *Journal of applied physics*, 25.5, 676-677.
- Nayak, P. ..., Mahesh, S., Snaith, H., & Cahen, D. (2019). Photovoltaic solar cell technologies: analysing the state of the art. *Nature Reviews Materials*, 4.4, 269-285.
- Kayes, B. M., Nie, H., Twist, R., Spruytte, S. G., Reinhardt, F., Kizilyalli, I. C., & Higashi, G. S. (2011). 27.6 % Conversion efficiency, a new record for single-junction solar cells under 1 sun illumination. *2011 37th IEEE Photovoltaic Specialist Conference*.
- Bailie, C. D. (2015). *Polycrystalline Tandem Photovoltaics*. Stanford University.
- Bremner, S., Levy, M., & Honsberg, C. B. (2008). Analysis of tandem solar cell efficiencies under AM1.5G spectrum using a rapid flux calculation method. *Progress in photovoltaics: Research and Applications*, 225-233.
- Martinho, F. (2021). Challenges for the future of tandem photovoltaics on the path to terawatt levels: a technology review. *Energy & Environmental Science*, 3840-3871.
- Fortunato, E., Ginley, D., Hosono, H., & Paine, D. C. (2007). Transparent conducting oxides for photovoltaics. *MRS bulletin*, 242-247.
- Kalowekamo, J., & Baker, E. (2009). Estimating the manufacturing cost of purely organic solar cells. *Solar energy*, 1224-1231.

- Lien, S. (2010). Characterization and optimization of ITO thin films for application in heterojunction silicon solar cells. *Thin Solid Films*, S10-S13.
- Mryasov, O., & Freeman, A. (2001). Electronic band structure of indium tin oxide and criteria for transparent conducting behavior. *Physical Review B*, 233111.
- Dekkers, J. M. (2007). Transparent conducting oxides on polymeric substrates by pulsed laser deposition.
- Hamberg, I., & Granqvist, C. G. (1986). Evaporated Sn-doped In₂O₃ films: Basic optical properties and applications to energy-efficient windows. *Journal of Applied Physics*, R123-R160.
- Köstlin, H., Jost, R., & Lems, W. (1975). Optical and electrical properties of doped In₂O₃ films. *Physica status solidi (a)*, 87-93.
- Gupta, L., A., M., & Srivastava, P. (1989). Band gap narrowing and the band structure of tin-doped indium oxide films. *Thin solid films*, 33-44.
- Woollam, J., McGaham, W., & Johs, B. (1994). Spectroscopic ellipsometry studies of indium tin oxide and other flat panel display multilayer materials. *Thin solid films*, 44-46.
- Delahoy, A., & Guo, S. (2011). Transparent conducting oxides for photovoltaics. *Handbook of Photovoltaic Science and Engineering*, 716-796.
- Bett, A. J., Winkler, K. M., Bivour, M., Cojocar, L., Kabakli, O. S., Schulze, P. S., & Goldschmidt, J. C. (2019). Semi-transparent perovskite solar cells with ITO directly sputtered on Spiro-OMeTAD for tandem applications. *ACS applied materials & interfaces*, 45796-45804.
- Leem, J. W., & Su, J. (2011). Glancing angle deposited ITO films for efficiency enhancement of a-Si: H/ μ c-Si: H tandem thin film solar cells. *Optic express*, A258-A269.
- Bush, K. A., Palmstrom, A. F., Yu, Z. J., Boccard, M., Cheacharoen, R., Mailoa, J. P., & McGehee, M. D. (2017). 23.6%-efficient monolithic perovskite/silicon tandem solar cells with improved stability. *Nature Energy*, 1-7.
- Zhang, D., Najafi, M., Zardetto, V., Dörenkämper, M., Zhou, X., Veenstra, S., & Andriessen, R. (2018). High efficiency 4-terminal perovskite/c-Si tandem cells. *Solar Energy Materials and Solar Cells*, 1-5.
- Song, Z., Werner, J., Shrestha, N., Sahli, F., De Wolf, S., Niesen, B., & Heben, M. J. (2016). Probing photocurrent nonuniformities in the sub-cells of monolithic perovskite/silicon tandem solar cells. *The Journal of Physical Chemistry Letters*, 5114-5120.

- Werner, J., Geissbühler, J., Dabirian, A., Nicolay, S., Morales-Masis, M., Wolf, S. D., & Ballif, C. (2016). Parasitic absorption reduction in metal oxide-based transparent electrodes: application in perovskite solar cells. *ACS applied materials & interfaces*, 17260-17267.
- Liu, N., Wang, L., Xu, F., Wu, J., Song, T., & Chen, Q. (2020). Recent progress in developing monolithic perovskite/Si tandem solar cells. *Frontiers in Chemistry*, 603375.
- Green, M., & Keevers, M. (1995). Optical properties of intrinsic silicon at 300 K. *Progress in Photovoltaics*, 189-192.
- Das, D., & Karmakar, L. (2019). Further optimization of ITO films at the melting point of Sn and configuration of Ohmic contact at the c-Si/ITO interface. *Applied Surface Science*, 16-24.
- Slotboom, J., & De Graaf, H. (1976). Measurements of bandgap narrowing in Si bipolar transistors. *Solid-State Electronics*, 857-862.
- Polyanskiy, M. (2022). *Refractive Index Database*. Retrieved from www.refractiveindex.info